



JP9612187

ISSN 0915-0313

NIFS--432  
JP9612187

NATIONAL INSTITUTE FOR FUSION SCIENCE

Magnetohydrodynamic Simulation on  
Co- and Counter-helicity Merging of  
Spheromaks and Driven Magnetic Reconnection

T.-H. Watanabe, T. Sato and T. Hayashi

(Received - July 24, 1996 )

NIFS-432

Aug. 1996

**RESEARCH REPORT**  
**NIFS Series**

*R*

1-1-1 HONDA TOWN, JAPAN

This report was prepared as a preprint of work performed as a collaboration research of the National Institute for Fusion Science (NIFS) of Japan. This document is intended for information only and for future publication in a journal after some rearrangements of its contents.

Inquiries about copyright and reproduction should be addressed to the Research Information Center, National Institute for Fusion Science, Nagoya 464-01, Japan.

# Magnetohydrodynamic Simulation on Co- and Counter-helicity Merging of Spheromaks and Driven Magnetic Reconnection

T.-H. Watanabe, T. Sato, T. Hayashi

Theory and Computer Simulation Center

National Institute for Fusion Science, Nagoya 464-01, Japan

## Abstract

A magnetohydrodynamic relaxation process of spheromak merging is studied by means of an axi-symmetric numerical simulation. As a result of counter-helicity merging, a field-reversed configuration is obtained in the final state, while a larger spheromak is formed after co-helicity merging. In the counter-helicity case, a clear pressure profile of which iso-surfaces coincide with flux surfaces is generated by thermal transport of a poloidal flow that is induced by driven reconnection. It is also found that a sharp pressure gradient formed at the edge of a current sheet causes a bouncing motion of spheromaks. According to the bounce motion, the reconnection rate changes repeatedly. As is shown by the TS-3 experiments, furthermore, strong acceleration of a toroidal flow and reversal of a toroidal field are observed in the counter-helicity merging.

**Key words :** spheromak, FRC, magnetic reconnection, MHD simulation

# I Introduction

Coalescence process of spheromaks has been experimentally studied using TS-3 device in Univ.Tokyo<sup>1-5</sup>. In the TS-3 experiments, it is shown that an FRC (field-reversed configuration) is formed after counter-helicity merging where two spheromaks have anti-parallel magnetic helicity, while a larger spheromak is obtained after co-helicity merging of spheromaks with the same helicity. In the counter-helicity case, driven reconnection causes strong heating and acceleration of ions and reversal of the toroidal field. The counter-helicity merging gives not only a potential method of slow formation of the FRC, but also a remarkable example for studying magnetic reconnection and MHD (magnetohydrodynamic) relaxation with finite pressure. It is noteworthy that the formation of pressure profile in the FRC can not be explained by the Taylor's relaxation theory<sup>6,7</sup> where a zero- $\beta$  plasma (or a uniform pressure profile) is assumed.

The first MHD simulation on the spheromak merging was carried out more than ten years ago for the co-helicity case in the zero- $\beta$  limit<sup>8</sup>. In the co-helicity merging, a larger spheromak is formed through the driven reconnection. The simulation result agrees well with the Taylor's theory. Recently, we made preliminary simulation studies on the counter-helicity merging in an axi-symmetric system, and confirmed that the final state in the counter-helicity case was the FRC<sup>9,10</sup>. Nevertheless, dynamic processes of spheromak merging have not yet been fully revealed.

In this paper, we will study the co- and counter-helicity merging of spheromaks using an axi-symmetric MHD simulation code with high spatial resolution. We will focus our attention to find how the plasma pressure is confined in the FRC in the counter-helicity case, and how the spheromak merging with a finite- $\beta$  effect develops through the driven magnetic reconnection. Comparison of the simulation results with the experimental evidences will help us to understand physical processes of spheromak merging.

We will show our simulation model in the next section. Overviews of simulation results

for the counter- and co-helicity merging are given in sections III A and B, respectively. In sections III C to E, we will present more detailed results, that is, a finite-pressure effect on magnetic reconnection, spontaneous confinement of pressure in the FRC, and toroidal oscillation of a reconnected magnetic loop. The results are summarized in the last section.

## II Simulation Model

To study merging processes of spheromaks, we solve the MHD equations for a finite- $\beta$  plasma. Governing equations are as follows:

$$\rho \frac{d\mathbf{v}}{dt} = -\nabla p + \mathbf{j} \times \mathbf{B} + \mu(\nabla^2 \mathbf{v} + \frac{1}{3}\nabla(\nabla \cdot \mathbf{v})), \quad (1)$$

$$\frac{1}{(\gamma - 1)} \frac{dp}{dt} = -\frac{\gamma}{\gamma - 1} p \nabla \cdot \mathbf{v} + \eta \mathbf{j}^2 + \Phi, \quad (2)$$

and

$$\frac{\partial \mathbf{B}}{\partial t} = -\nabla \times \mathbf{E}. \quad (3)$$

Here,  $\mathbf{j}$ ,  $\mathbf{E}$ ,  $\Phi$ , and  $e_{ij}$  are given by

$$\mathbf{j} = \nabla \times \mathbf{B}, \quad (4)$$

$$\mathbf{E} = -\mathbf{v} \times \mathbf{B} + \eta \mathbf{j}, \quad (5)$$

$$\Phi = 2\mu \left( e_{ij} e_{ij} - \frac{1}{3}(\nabla \cdot \mathbf{v})^2 \right), \quad (6)$$

and

$$e_{ij} = \frac{1}{2} \left( \frac{\partial v_i}{\partial x_j} + \frac{\partial v_j}{\partial x_i} \right). \quad (7)$$

$\gamma$ ,  $\mu$ , and  $\eta$  are ratio of the specific heats ( $\gamma = 5/3$ ), viscosity ( $\mu = 1 \times 10^{-4}$ ), and resistivity ( $\eta = 1 \times 10^{-4}$ ). In simulation runs given in section III C, we will change the value of  $\gamma$  as a physical parameter.  $\Phi$  is a dissipation function due to the viscosity, and  $e_{ij}$  denotes a rate-of-strain tensor. Other notations are standard. All of physical quantities are normalized by typical Alfvén speed  $V_A$ , mass density  $\rho$ , and radius of the cylindrical

vessel  $R_V$ . Here,  $\rho$  is assumed to be uniform and constant in time for simplicity. Time-integration of  $\mathbf{B}$ ,  $\mathbf{v}$ , and  $p$  is calculated by the fourth-order Runge-Kutta-Gill method. Spatial derivatives are computed by the second-order finite difference.

The present simulation system is schematically plotted in Fig.1. A cylindrical vessel is set in  $0 < r < 1$  and  $-2 < z < 2$ . We assume the axi-symmetry, and carry out numerical simulations in a two-dimensional poloidal plane which is shown by shade in Fig.1. The simulation domain is represented by spatial grid points of  $289 \times 1153$  in  $(r, z)$  coordinates. To check convergence against the grid spacing, we have also performed a simulation using finer grid points of  $577 \times 2305$ , and have obtained the same results with what will be shown in this paper. We use a perfect conducting boundary at the vessel wall. Velocity is fixed to zero on the boundary, while pressure is calculated so that no thermal flux passes through the wall. Initially, a homogeneous zero- $\beta$  plasma fills the simulation domain, such as  $\rho = 1$ ,  $p = 0$ , and  $\mathbf{v} = 0$ . An initial condition for magnetic field is given as follows. At first we set a pair of toroidal currents  $j_\varphi$  centered at  $z = \pm 0.75$ . Each of the toroidal current pattern is given by the Hill's vortex solution<sup>11</sup> of  $\nabla \times \mathbf{B} = \lambda \mathbf{B}$  ( $\lambda = \text{constant}$ ) with radius of  $a = 0.5$ . Direction of the toroidal currents are set to be the same (negative  $\varphi$  direction) in order to make the spheromaks merge. Secondly, to determine  $B_r$  and  $B_z$  consistently with  $j_\varphi$ , we numerically solve

$$-\nabla^2 A_\varphi + A_\varphi/r^2 = j_\varphi \quad (8)$$

where  $A_\varphi$  means  $\varphi$  component of the vector potential. A boundary condition for  $A_\varphi$  is

$$\frac{1}{r} \frac{\partial}{\partial r} (r A_\varphi) = B_z = -\frac{2C}{x_1} \sin x_1 \quad \text{at } r = 1, \quad (9)$$

and

$$-\frac{\partial A_\varphi}{\partial z} = B_r = 0 \quad \text{at } z = \pm 2. \quad (10)$$

Here,  $x_1$  denotes the first zero of the first-order spherical Bessel function, that is,  $x_1 =$

4.493, and we set the constant  $C = 2.5$ . Finally, the toroidal field  $B_\varphi$  is given by

$$B_\varphi = \pm C x_1 A_\varphi / a \quad \text{for} \quad A_\varphi \leq 0 \quad (11)$$

or

$$B_\varphi = 0 \quad \text{for} \quad A_\varphi > 0 \quad . \quad (12)$$

Each of  $B_\varphi$  in the two spheromaks has different signs in the counter-helicity case but has the same negative sign in the co-helicity case. The maximum intensity of  $B_\varphi$  at  $t = 0$  is about 1.1. The initial configuration of the magnetic field does not satisfy the force-free condition, although the current density in perpendicular to the magnetic field is much weaker than the parallel one. This is because each of the spheromak feels the poloidal field of the other one. Then, the spheromaks attract each other by the Lorentz force and start to merge at  $z = 0$ .

### III Simulation Results

#### A An Overview of Counter-helicity Merging

Here, we present an overview of simulation results for the counter-helicity merging of spheromaks. Contours of the poloidal flux  $\Psi$  at different time steps are shown in Fig.2, where only negative regions are plotted in the poloidal plane. The outermost line corresponds to  $\Psi = 0$ . Thus, separatrixes locate at cross-points of  $r = 0$  and  $\Psi = 0$ . In the initial stage of simulation ( $t < 5\tau_A$ ;  $\tau_A$  denotes Alfvén transit time), one can see that the two spheromaks approach to the  $z = 0$  line. Then, the driven magnetic reconnection<sup>12</sup> takes place at  $z = 0$ , where a reconnection point (X-point defined as a saddle point of the poloidal flux contour) and a current sheet are formed between the two spheromaks. As time goes, the reconnection proceeds deeper into the un-merged region, and the reconnected flux increases. The merging of spheromaks has been completed at  $t = 25\tau_A$ .

The toroidal magnetic field is plotted in Fig.3 by solid and dashed contours. As the merging continues, the anti-parallel toroidal field annihilates and finally disappears. Thus, a large amount of toroidal field energy is released in the counter-helicity merging. The final configuration with no toroidal field is an FRC. In addition, one can see that the toroidal field is reversed around un-merged flux surfaces (see  $t = 10$  and  $15\tau_A$ ). The reversal of the toroidal field is observed also in the TS-3 experiments and is considered to be closely related with a toroidal flow<sup>1,4</sup>. A physical mechanism of the field reversal will be elucidated in section III E.

Fig.4 shows pressure profiles at different time steps. In the merging phase ( $t = 10$  and  $15\tau_A$ ) the pressure peaks at  $z = 0$ , where the reconnection takes place and the magnetic energy is converted to the thermal energy. The increased pressure profile is broadened into the system along the reconnected flux surfaces. A clear pressure profile has been formed after merging, though the thermal conduction effect is not taken into account. In the final state, the iso-pressure surfaces coincide with the flux surfaces, in other words, the poloidal field supports the pressure gradient. Furthermore, it should be noted that most of the increased pressure is confined in the FRC.

Temporal plots of magnetic, kinetic, and thermal energies in the cylindrical vessel are shown in Fig.5(a). About 20 % of the initial magnetic energy decreases in the counter-helicity merging from  $t = 7$  to  $20\tau_A$ . Most of the released magnetic energy is converted to the thermal energy. After  $t = 20\tau_A$ , all of the energies are nearly constant, and the system approaches to a steady state. One can find three faint peaks in the time evolution of the kinetic energy (at  $t = 9, 15,$  and  $19\tau_A$ ). It means that acceleration of a plasma flow, namely, the driven reconnection is enhanced three times, repeatedly. Detailed results found in the time evolution of the driven reconnection are given in section III C.

In Fig.5(b), we have plotted the parallel and perpendicular components of current density averaged inside of the separatrixes ( $\Psi < 0$ ). As the spheromaks continue to



merge, the parallel current which is the dominant component at  $t = 0$  decreases, but the perpendicular one increases. After the merging, at  $t = 40\tau_A$ , the perpendicular current has grown about five times larger than the parallel one.

Time evolution of the spatially-averaged force  $\langle |\mathbf{j} \times \mathbf{B} - \nabla p| \rangle$  is presented in Fig.5(c), where one can see three major peaks in correspondence to the three peaks of the kinetic energy found in Fig.5(a). Moreover, the averaged force approaches to zero after the merging. Namely, the MHD equilibrium condition of  $\mathbf{j} \times \mathbf{B} = \nabla p$  is nearly satisfied. From the above simulation results, one can conclude that an FRC is spontaneously formed after the counter-helicity merging of spheromaks.

## B An Overview of Co-helicity Merging

Changing the polarity of the toroidal magnetic field in the lower spheromak, we have carried out a simulation for the co-helicity case. Contour plots of poloidal flux, toroidal field, and pressure for the co-helicity merging are, respectively, given in Figs.6-8 in the same format as Figs.2-4. Also in this case, two spheromaks attract each other and, then, start to merge through the driven reconnection. Opposite to the counter-helicity case, the toroidal field remains after merging. Thus, the final configuration is a spheromak (or a prolomak). This implies that released magnetic energy, thus, the increased thermal energy, in the co-helicity merging should be less than those in the counter-helicity case. The pressure profiles shown in Fig.8 reflect this fact. A finite pressure gradient is, however, formed even in this case.

Figs.9(a)-(c) show time evolutions of energies, parallel and perpendicular current density, and an averaged force, as same as Fig.5(a)-(c). The magnetic energy slightly decreases at about  $t = 8\tau_A$  due to the reconnection. After completion of the merging at  $t = 20\tau_A$ , the magnetic energy continues to decrease owing to the resistive dissipation, while the thermal energy increases gradually. A remarkable difference from the counter-helicity case is

found in magnitudes of the parallel and perpendicular currents in Fig.9(b). Throughout the merging process, the parallel current exceeds the perpendicular component. Thus, the final state is a spheromak type. Nevertheless, existence of the perpendicular current means that the finite pressure gradient is balanced with the Lorentz force in the final state, as is confirmed in Fig.9(c).

### C A Finite-Pressure Effect on Magnetic Reconnection

As has been shown in Fig.5(a), in the counter-helicity merging, the magnetic energy rather rapidly decreases at  $t = 8, 14,$  and  $18\tau_A$ . Namely, the magnetic reconnection is enhanced three times, repeatedly. Fig.10 shows temporal plots of three physical quantities measured at the X-point, such as the current density in  $r$  and  $\varphi$  directions and the pressure. In the bottom panel, radial position of the X-point is plotted versus time. After completion of the merging, we have picked up data on the magnetic axis. Viewing the plots in Fig.10, one can see that relaxation stage of the counter-helicity merging is apparently divided into two phases such as active and inactive ones. In the active phase, the magnetic reconnection is driven by a plasma flow in  $z$  direction, and the peak current intensity at the X-point (reconnection current) is extremely large, more than 100. Here we remind the reader that the averaged current density at  $t = 0$  is only 6 as is shown in Fig.5(b). According to the current peaking at the X-point, the pressure is increased by the enhanced Joule heating, while it decreases in the inactive phase. In intervals of the current peaking, namely in the inactive phase, the  $r$  (poloidal) component of the reconnection current decreases, and the  $\varphi$  (toroidal) component is reversed. This implies not only that the spheromak merging is stopped, but also that the merged flux is re-separated by another reconnection driven in  $r$  direction. In other words, the two spheromaks repeat a bouncing motion.

The time evolutions of the current density shown in Fig.10 clearly reflect the mag-

netic field configuration of counter-helicity spheromaks. A spheromak has only poloidal field at the edge, while only the toroidal field exists on the magnetic axis. In the initial stage of merging, the poloidal field dominates in the reconnection process, and thus, the toroidal reconnection current firstly increases. In the final stage of merging, however, the anti-parallel toroidal field governs the reconnection process, namely, the radial reconnection current becomes much larger than the toroidal one. Incidentally, one can see that, according to radial shift of the X-point, the toroidal current starts to decrease earlier than the radial component. In the active phase, the X-point locates at about  $r = 0.3$ , while it shifts to  $r = 0.5$  in the inactive phase. When the active phase begins again, the X-point immediately returns to its original position. The shift of the X-point and the decrease of the toroidal reconnection current correspond to shortening of the current sheet between the spheromaks.

In Fig.11 we have plotted contours of the poloidal flux from  $t = 8$  to  $12\tau_A$  with high-time resolution. In the first active phase of reconnection at  $t = 8\tau_A$ , a so-called Y-type current sheet is formed in a contact layer of spheromaks. However, radial length of the current sheet becomes shorter and shorter, as the toroidal reconnection current decreases ( $t = 9 \sim 10\tau_A$ ). At  $t = 10\tau_A$ , the reconnected flux surfaces are largely bent, and the reconnected flux is accumulated between two spheromaks where one can find a local pressure enhancement (see Fig.4). Thus, the current sheet shape becomes an X-type, and the spheromaks are slightly bounced back. In the second active phase ( $t = 12\tau_A$ ), the Y-type current sheet is formed again. The transition of current sheet shape from the Y- to X-type has been found also in a two-dimensional MHD simulation on driven reconnection started from a Harris-type equilibrium<sup>13</sup>. Thus, the oscillating feature related with the bouncing motion of spheromaks seems to reflect an elementary process of driven reconnection.

The above simulation results suggest that the local pressure enhancement in the vicin-

ity of the X-point plays an essential role in triggering the bouncing motion of spheromaks, while the compressed field repelled the island plasma in the incompressible MHD simulation on coalescence of magnetic islands by Biskamp<sup>14</sup>. To confirm the effect of pressure, cross-sectional plots of pressure, pressure gradient, and the Lorentz force at  $z = 0$  are given in Fig.12. It is noteworthy that, at  $t = 8\tau_A$ , sharp pressure gradients which decelerate an outward plasma flow from the X-point are generated at the inner and outer edges of the Y-type current sheet (near at  $r = 0.2$  and  $0.5$ , respectively), and that position of the pressure gradients moves toward the X-point in accordance with shortening of the current sheet. Due to the geometrical effect of the cylindrical vessel, the pressure is accumulated more at the inner edge than the outer one. In the inactive phase ( $t = 10\tau_A$ ), the pressure profile is broadened. This result shows that the local enhancements of pressure at the edges of the current sheet control the current sheet length and repel the attracting motion of spheromaks. Thus, the bouncing motion is triggered, and the reconnection rate decreases.

From the above simulation results, we can deduce a following scenario on the dynamic change of the reconnection rate and the bouncing motion of spheromaks. The magnetic reconnection driven by the attracting motion of spheromaks enhances the Joule heating at  $z = 0$ . Then, a high-pressure layer is formed between the two spheromaks. The increased pressure is transported by an outward plasma flow that is induced by the driven reconnection. When the thermal transport is inefficient with respect to the enhanced Joule heating, the pressure is accumulated on down-stream sides of the X-point. Then, the sharp pressure gradients which decelerate the outward flow are formed at the edges of the current sheet. Hence, the pressure is accumulated more. Since the outward flow is stopped, the reconnected fluxes are not transferred out of the contact layer of spheromaks, then, the current sheet becomes the X-type. The transition of the current sheet shape from the Y- to X-type means that a vertical plasma motion driving the reconnection

is weakened, and that the spheromaks are bounced. Therefore, the reconnection rate is decreased, and the inactive phase begins. When the pressure gradients become sufficiently weak due to the vertical expansion and the convective thermal transport, the reconnection is activated again by the attracting force of spheromaks. Thus, the X-point returns to the original position, and the Y-type current sheet is formed. Repeating the above process, the reconnection rate changes oscillatory.

We have also performed three simulation runs changing the value of  $\gamma$  from  $3/2$  to  $7/3$  for the counter-helicity case. For larger  $\gamma$ , the reconnection rate will be saturated at a lower level<sup>15</sup>, since the pressure increases more sensitively to a thermal production rate. Temporal plots of the reconnection current are given in Fig.13 for  $\gamma = 3/2, 5/3, 6/3$ , and  $7/3$ . Solid and dashed lines represent  $r$  and  $\varphi$  components, respectively. One can see that intensity of the reconnection current, namely, the magnetic reconnection rate, largely depends on  $\gamma$ . For larger  $\gamma$ , the current density increase saturates at a lower level, and the merging of spheromaks takes longer. In the case of  $\gamma = 7/3$ , the merging has not yet been completed at the end of the simulation ( $t = 35\tau_A$ ), although the active phase was repeated six times.

The oscillation of reconnection rate is also found in the co-helicity merging with larger  $\gamma$  as is shown in Fig.14. Only the toroidal reconnection current appears in the co-helicity case because of the same toroidal field configuration in the two spheromaks. Also in this case, as  $\gamma$  becomes larger, growth of the reconnection current is suppressed at a lower level, and the oscillation becomes clearer. For the cases of  $\gamma = 3$  and  $4$ , the active phase is repeated three times.

The above simulation results support our scenario that the local pressure enhancement causes the decrease of the reconnection rate and, exciting the bouncing motion of spheromaks, prevents progress of the merging.

## D Spontaneous Pressure Confinement in the FRC

In the counter-helicity case, the global pressure profile of which gradient balances with the Lorentz force is spontaneously formed, as a natural consequence of the spheromak merging. A formation process of the pressure profile is described in this section. Fig.15 shows time evolutions of pressure for the counter-helicity case observed at five different points, that is,  $r = 0.3$  and  $z = 0.6, 0.45, 0.3, 0.15,$  and  $0$ , respectively. Here,  $\gamma = 5/3$ . Corresponding to the start of reconnection, the pressure is increased at  $z = 0$  by the Joule heating. After a while, at  $t = 12\tau_A$ , the pressure rises at  $z = 0.6$ , although it is away from the X-point. As the observation point approaches to the X-point, except  $z = 0$ , pressure increases later and later. Hence, as is shown in Fig.4, a hollow pressure profile is temporarily formed.

A probable mechanism to explain the formation of the pressure profile is thermal transport due to a poloidal flow, namely, convective transport and compressive heating. The driven reconnection induces a poloidal flow which diverges from the X-point and can transport the increased thermal energy. If the poloidal flow is parallel to flux surfaces, the pressure will increase along the reconnected flux surfaces due to the convection and/or the compression. As the merging proceeds, the poloidal flow makes the plasma heating along the inner flux surfaces. Moreover, the compressive heating can adjust the pressure profile so that the pressure gradient balances with the Lorentz force. Therefore, the pressure profile, of which iso-surfaces coincide with the flux surfaces, can be generated spontaneously.

As will be explained in detail in the next section, in the counter-helicity merging a reconnected magnetic loop oscillates in the toroidal direction, relaxing excessive magnetic tension and accelerating a toroidal flow. Thus, according to the toroidal oscillation, the magnetic field is sheared between reconnected and un-reconnected flux surfaces, where a sheet current is induced. The Joule heating due to the sheet current and the viscous

damping of the toroidal flow also contribute to increase the thermal energy. Nevertheless, the thermal transport of a poloidal flow is indispensable to equalize the pressure along flux surfaces.

To check the above hypothesis, we have plotted poloidal flow patterns at different time steps in Fig.16. At  $t = 5\tau_A$ , a plasma flow toward  $z = 0$  starts to make the spheromaks merge. In the merging phase, at  $t = 10\tau_A$ , the flow pattern is rather complicated. Comparing Fig.16 with Fig.2, one can find a poloidal flow component around the un-merged flux surfaces. At  $t = 15\tau_A$ , the poloidal flow is generated around inner flux surfaces, as the merging proceeds deeper. Fig.17 shows historical plots of the pressure and its source terms observed at  $r = 0.3$  and  $z = 0.6$ . In the top panel, time evolution of the pressure is re-plotted for a reference. Convection,  $-\mathbf{v} \cdot \nabla p$ , compression,  $-\gamma p \nabla \cdot \mathbf{v}$ , Joule heating,  $(\gamma - 1)\eta \mathbf{j}^2$ , and viscous heating,  $(\gamma - 1)\Phi$ , terms are respectively shown in Fig.17. As is expected, both the convection and compression terms are enhanced according to the increase of pressure. The Joule and viscous heating terms are minor components. Therefore, it is concluded that the pressure profile is spontaneously generated by the thermal transport of the poloidal flow that is induced by the driven reconnection.

## E Toroidal Oscillation of a Magnetic Loop

During the counter-helicity merging of spheromaks, the toroidal field is reversed on reconnected flux surfaces (see Fig.3). Mechanism of the field reversal has been considered as follows<sup>1,4</sup>. Because of the counter-helicity configuration with the anti-parallel toroidal field, a just-reconnected magnetic loop is inclined with respect to a poloidal plane, in other words, is elongated in toroidal direction. The elongated magnetic loop causes strong acceleration of a toroidal flow (a slingshot effect). If the toroidal flow speed is sufficiently large, the magnetic loop may overshoot an equilibrium position. Hence, the toroidal field is reversed and the magnetic loop oscillates in the toroidal direction (Alfvén oscillation).

In Fig.18(a), we have plotted a magnetic loop of  $\Psi = -5 \times 10^{-3}$  which is just-reconnected at  $t = 8\tau_A$ . One can see that the magnetic loop is actually elongated in  $\varphi$  direction, and that its configuration is quite different from the FRC with no toroidal field. Thus, excessive tension of the magnetic loop should be relaxed, and the plasma is accelerated in toroidal direction. In the relaxation process of the excessive magnetic tension, therefore, one will find the reversal of toroidal field.

To examine the toroidal oscillation of the magnetic loop, we have traced motion of two representative points on the loop which are marked by A and B in Fig.18(a). Solid line in Fig.18(b) indicates elongation of the magnetic loop defined by a relative toroidal angle of the two points, A and B, that is,  $\varphi_B - \varphi_A$ . Toroidal oscillation of the magnetic loop is clearly found in the figure. When the elongation angle becomes negative, the toroidal field is reversed. The oscillation is gradually damped by the finite resistivity and viscosity. Then, the elongation angle approaches to zero, namely, the toroidal field vanishes along the magnetic loop. Dotted and Dashed lines in Fig.18(b), respectively, show toroidal flow speed at points-A and -B. The toroidal flow at the point-A is strongly accelerated up to  $0.7 V_A$ , where  $V_A$  is the typical Alfvén speed. Corresponding to the field line motion, the toroidal flow changes its direction because of the sling shot effect. Oscillations found in the flow speed lead by  $\pm\pi/2$  in phase to that of the magnetic loop. Thus, it is summarized that the Alfvén coupling of the magnetic loop motion and the toroidal flow causes the toroidal acceleration and the field reversal.

## IV Summary and Discussion

We have investigated the coalescence process of two spheromaks for the co- and counter-helicity cases, employing the axi-symmetric MHD simulation code. Obtained results are summarized as follows:



1. In the counter-helicity merging of zero- $\beta$  spheromaks, an FRC is formed through the driven magnetic reconnection which locally increases the thermal energy in the vicinity of the X-point, while a larger spheromak (or a prolomak) is obtained in the co-helicity case.
2. The increased thermal energy is transported by the poloidal flow which is generated by the driven reconnection. Hence, the pressure profile of which iso-surfaces coincide with the flux surfaces is spontaneously formed, though the thermal conduction effect is not taken into account in the present simulation. In the final state of the counter-helicity merging, most of the pressure is confined in the closed flux surfaces.
3. The driven magnetic reconnection is repeatedly enhanced in the merging process, according to the bouncing motion of spheromaks. The bouncing motion is triggered by the local enhancement of pressure that decelerates the outward plasma flow from the X-point and leads to the transition of the current sheet shape from the Y- to X-type.
4. The toroidal Alfvén oscillation of a reconnected magnetic loop is clearly demonstrated in the counter-helicity case. The toroidal field around the un-merged flux surfaces is temporarily reversed by the accelerated toroidal flow, as is shown by the TS-3 experiments.

The present simulation results are qualitatively consistent with the TS-3 experiments for the formation of the FRC, the reversal of toroidal field, and the acceleration of toroidal flow. The bouncing motion of spheromaks is, however, not clearly found in the counter-helicity merging experiments. Moreover, experimental estimation of the reconnection rate in the counter-helicity case is about three times higher than that in the co-helicity one<sup>1-5</sup>, while in the present simulation the co-helicity merging has been finished earlier than

the counter-helicity case. These discrepancies between the present simulations and the experiments may originate from differences in the viscosity and the thermal conductivity.

In order to examine an effect of the viscosity, we have performed two additional simulation runs with  $\mu = 3 \times 10^{-4}$  and  $1 \times 10^{-3}$ . In the case of  $\mu = 1 \times 10^{-3}$ , the oscillation of the reconnection rate does not clearly appear, and the current density at the X-point slowly evolves in time. On the other hand, the driven reconnection is enhanced three times in the case of  $\mu = 3 \times 10^{-4}$ . Although the present viscosity model is much simpler than that in real plasmas, it seems that for occurrence of the bouncing motion the viscosity is needed to be as weak as a flow pattern nearby the X-point is changed by the local pressure enhancement.

In the present simulations, the effect of thermal conduction is not taken into account, while the thermal transport due to the poloidal flow mainly contributes to form the pressure profile. If large parallel thermal conductivity is introduced in our simulations, the pressure will rapidly equalize itself along field lines due to the thermal conduction rather than the thermal transport by the poloidal flow. Then, the merging speed may be largely increased in the counter-helicity case, since the finite pressure effect would no longer cause the bouncing motion of spheromaks. We are now studying the effect of thermal conductivity on the spheromak merging. However, a simulation with the thermal conduction takes about 30 times longer computational time (approximately 30 hours on the NEC SX-3 system) than the present one. The simulation results, therefore, will be presented elsewhere.

In this study, we have assumed the axi-symmetry, and have carried out the two-dimensional simulations. To discuss about the minimum energy state after the coalescence of spheromaks, however, we should consider all of ideal instabilities in a full three-dimensional system. Although the  $n = 1$  tilt and/or shift modes may be unstable in the three-dimensional system, it can be stabilized by a center conductor<sup>16</sup>. We will investigate

a three-dimensional effect on the spheromak merging in future.

## **Acknowledgment**

One of the authors (T.-H.W.) would like to thank M.Yamada, R.M.Kulsrud, T.Ohkawa, A.Ishida, Y.Ono, M.S.Chu, S.-P.Zhu, and H.Kitabata for stimulating discussions and fruitful comments. Numerical computations in this study are performed on the NIFS Advanced Computing System for Complexity Simulation.

## References

- <sup>1</sup> M. Yamada, Y. Ono, A. Hayakawa, M. Katsurai, and F.W. Perkins, Phys. Rev. Lett., **65**, 721 (1990).
- <sup>2</sup> M. Yamada, F.W. Perkins, A.K. MacAulay, Y. Ono, and M. Katsurai, Phys. Fluids B, **3**, 2379 (1991).
- <sup>3</sup> Y. Ono, A. Morita, T. Itagaki, and M. Katsurai, Plasma Phys. Cont. Nucl. Fusion Res. 1992, 619 (1993).
- <sup>4</sup> Y. Ono, A. Morita, M. Katsurai, and M. Yamada, Phys. Fluids B, **5**, 3691 (1993).
- <sup>5</sup> Y. Ono, Trans. Fusion Tech., **27**, 369 (1995).
- <sup>6</sup> J.B. Taylor, Phys. Rev. Lett., **33**, 1139 (1974).
- <sup>7</sup> J.B. Taylor, Rev. Mod. Phys., **58**, 741 (1986).
- <sup>8</sup> T. Sato, Y. Oda, S. Otsuka, K. Katayama, and M. Katsurai, Phys. Fluids, **26**, 3602 (1983).
- <sup>9</sup> B. Dasgupta, T. Sato, T. Hayashi, K. Watanabe, and T.-H. Watanabe, Trans. Fusion Tech., **27**, 374 (1995).
- <sup>10</sup> T.-H. Watanabe, T. Sato, T. Hayashi, K. Watanabe, J. Plasma Fusion Res., **72**, 101, (1996) (in Japanese).
- <sup>11</sup> M.N. Rosenbluth and M.N. Bussac, Nucl. Fusion, **19**, 489 (1979).
- <sup>12</sup> T. Sato and T. Hayashi, Phys. Fluids, **22**, 1189 (1979).
- <sup>13</sup> H. Kitabata, Ph.D thesis, The Graduate University for Advanced Studies, Japan (1996).
- <sup>14</sup> D. Biskamp, Phys. Rep., **4**, 179 (1994) and references therein.
- <sup>15</sup> T. Sato, T. Hayashi, K. Watanabe, R. Horiuchi, M. Tanaka, N. Sawairi, and K. Kusano, Phys. Fluids B, **4**, 450 (1992).
- <sup>16</sup> T. Hayashi and T. Sato, Phys. Fluids, **28**, 3654 (1985).

## Figure Captions

FIG.1 Schematic plot of the simulation system in cylindrical coordinates  $(r, \varphi, z)$ . Shaded poloidal plane at  $\varphi = 0$  shows the two-dimensional simulation domain. Perfect conducting boundary is located at  $r = 1$  and  $z = \pm 2$ . At  $t = 0$ , two spheromaks with radius of  $a = 0.5$  are placed at  $z = \pm 0.75$ .

FIG.2 Contours of the poloidal flux at different time steps for merging of two spheromaks with anti-parallel helicity. Only negative parts are plotted for clarity. Contour interval is set to be  $2.5 \times 10^{-3}$ .

FIG.3 Same as FIG.2 but for the toroidal field contours with interval of 0.1. Solid and dotted lines show positive and negative components, respectively.

FIG.4 Same as FIG.2 but for the pressure contours with interval of  $2.5 \times 10^{-2}$ .

FIG.5 Time evolutions of (a) energies in the system, (b) the parallel and perpendicular currents, and (c) the spatially-averaged force.

FIG.6 Same as FIG.2 but for the co-helicity case.

FIG.7 Same as FIG.3 but for the co-helicity case.

FIG.8 Same as FIG.4 but for the co-helicity case.

FIG.9 Same as FIG.5 but for the co-helicity case.

FIG.10 Temporal plots of the radial and toroidal current density and the pressure observed at the X-point in the counter-helicity merging. The bottom panel shows radial position of the X-point.

FIG.11 Same as FIG.2 but at different time steps.

FIG.12 Cross-sectional plots of pressure at  $z = 0$  for  $t = 8, 9, 10\tau_A$ . Lower two graphs, respectively, show radial components of the pressure gradient and the Lorentz force at  $t = 8\tau_A$ .

FIG.13 Temporal plots of current density at the X-point for  $\gamma = 3/2, 5/3, 6/3,$  and  $7/3$  for the counter-helicity case. Solid and dashed lines show  $r$  and  $\varphi$  components, respectively.

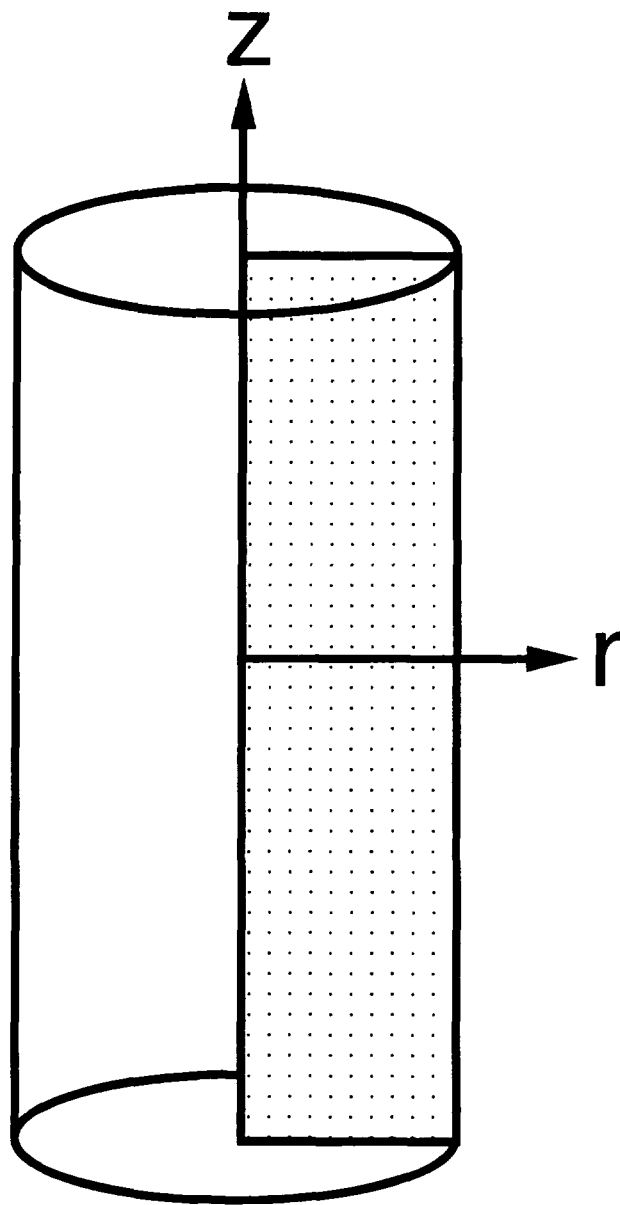
FIG.14 Same as FIG.13 but for the co-helicity merging with  $\gamma = 5/3, 2, 3,$  and  $4$ .



FIG.15 Time evolution of the pressure observed at  $r = 0.3$  and  $z = 0.6, 0.45, 0.3, 0.15,$  and  $0$  in the counter-helicity case.

FIG.16 Poloidal flow patterns at different time steps in the counter-helicity merging.

FIG.17 Temporal plots of the pressure, convection,  $-\mathbf{v} \cdot \nabla p$ , compression,  $-\gamma p \nabla \cdot \mathbf{v}$ , Joule heating,  $(\gamma - 1)\eta \mathbf{j}^2$ , and viscous heating,  $(\gamma - 1)\Phi$ , terms at  $r = 0.3$  and  $z = 0.6$  in the counter-helicity case.

FIG.18 Dynamic behavior of a reconnected magnetic loop in the counter-helicity merging. (a) Three dimensional plots of the magnetic loop of  $\Psi = -5 \times 10^{-3}$  in the cylindrical vessel at  $t = 8\tau_A$ . (b) Historical plots of the elongation of the magnetic loop defined by the relative toroidal angle  $\varphi_B - \varphi_A$  and the toroidal flow velocity at points-A and -B.



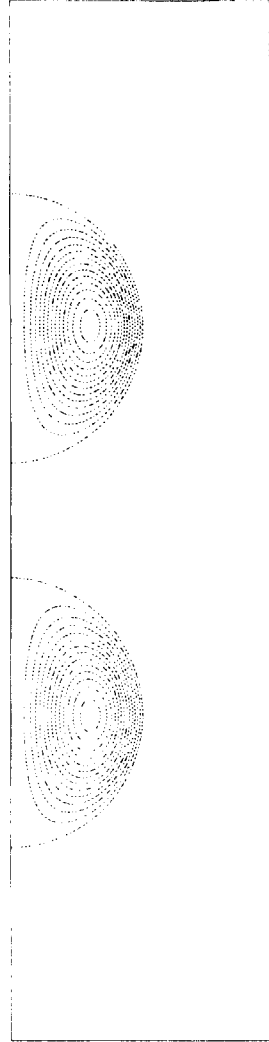
-  Perfect Conducting Vessel
-  2-D Simulation Domain

Wat anabe

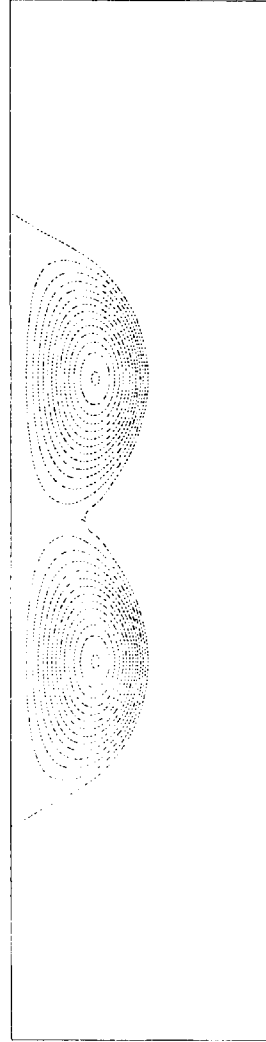
FIG.1

# Poloidal Flux (Counter-helicity Case)

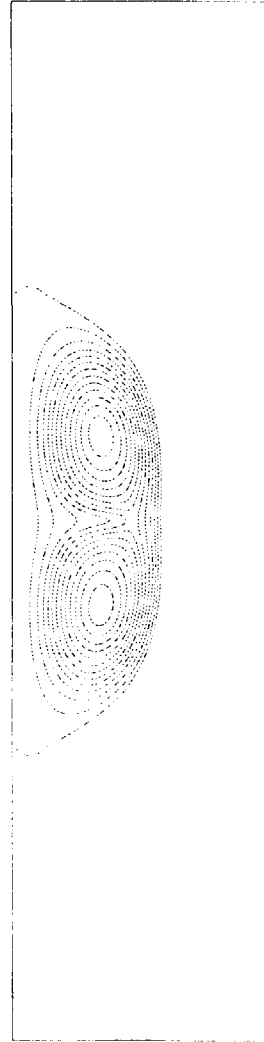
t = 0.00



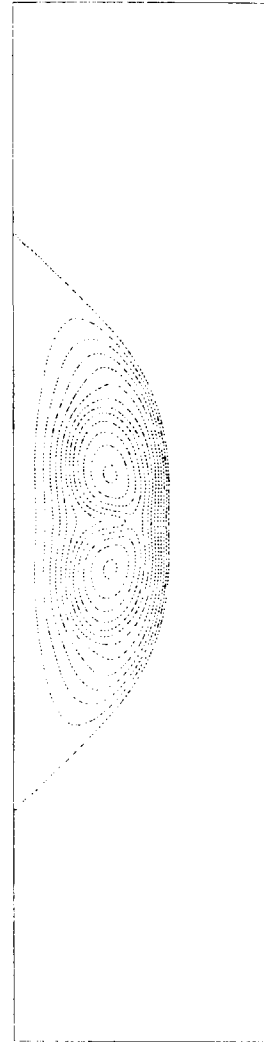
t = 5.00



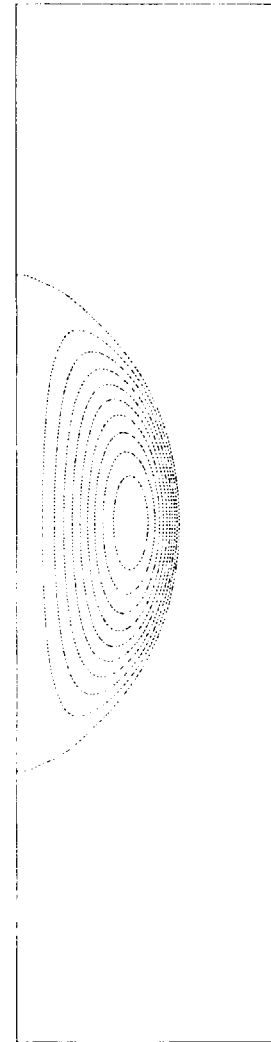
t = 10.00



t = 15.00



t = 40.00

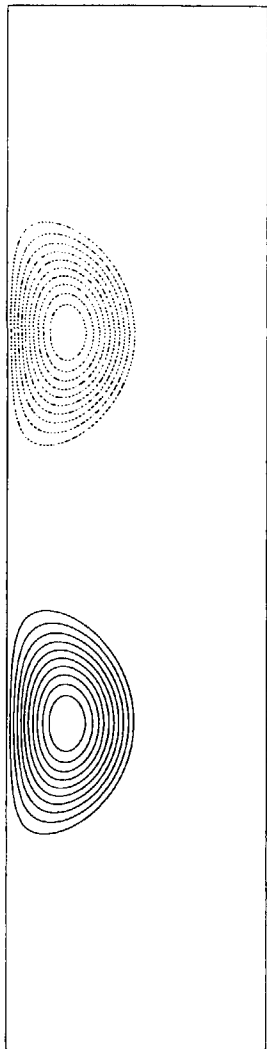


Wat anabe  
FIG.2

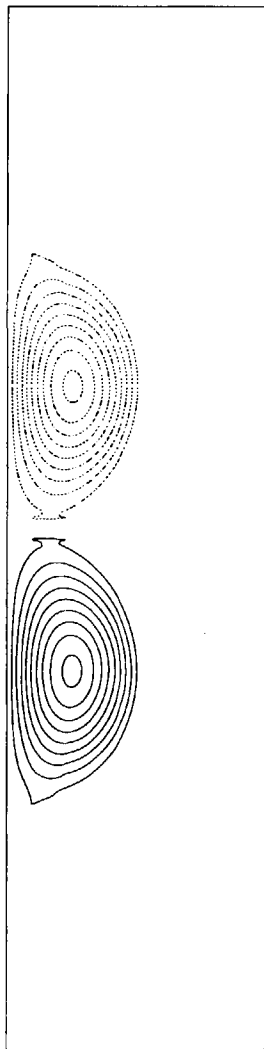


# Toroidal Field (Counter-helicity Case)

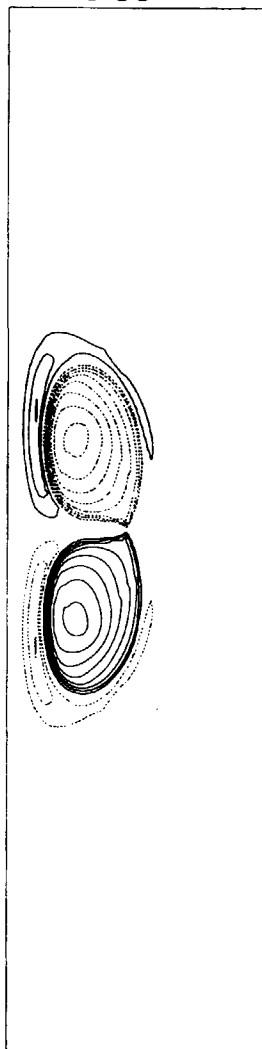
t = 0.00



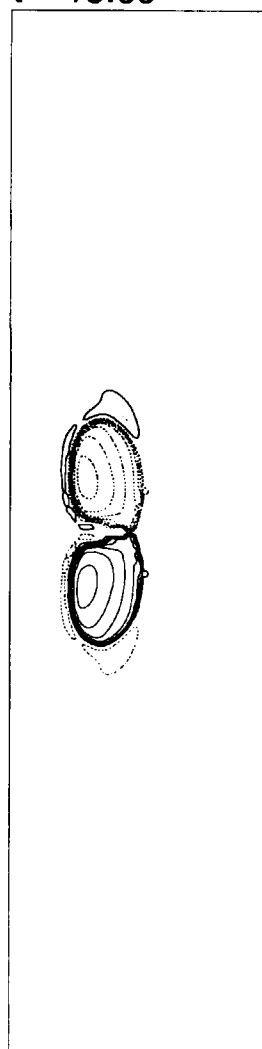
t = 5.00



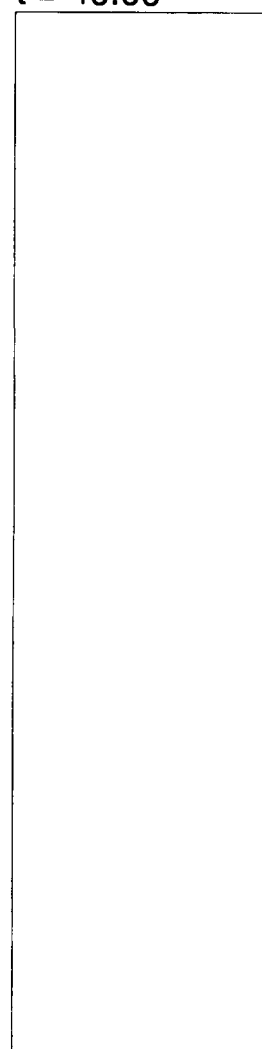
t = 10.00



t = 15.00



t = 40.00

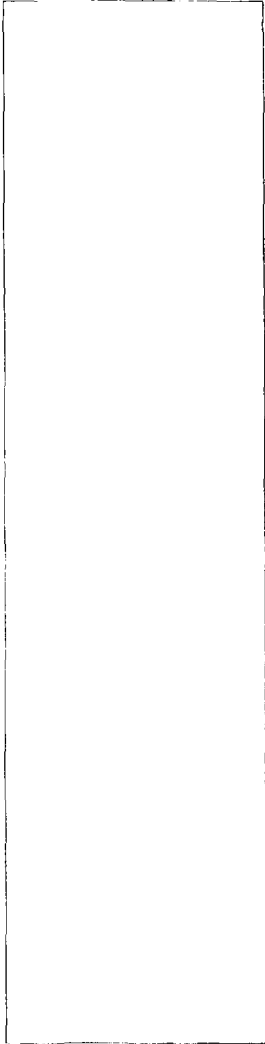


Wat anabe

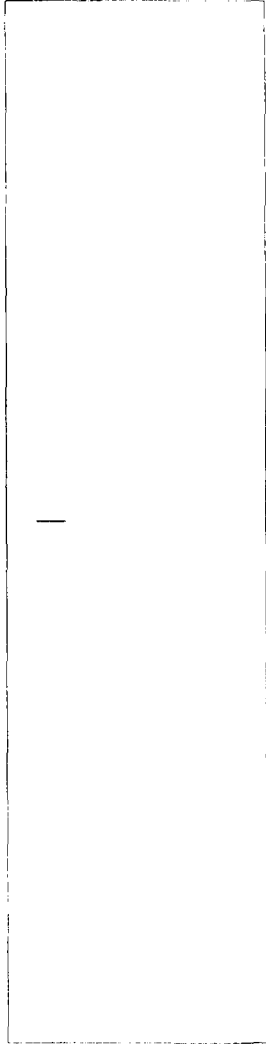
FIG.3

Pressure (Counter-helicity Case)

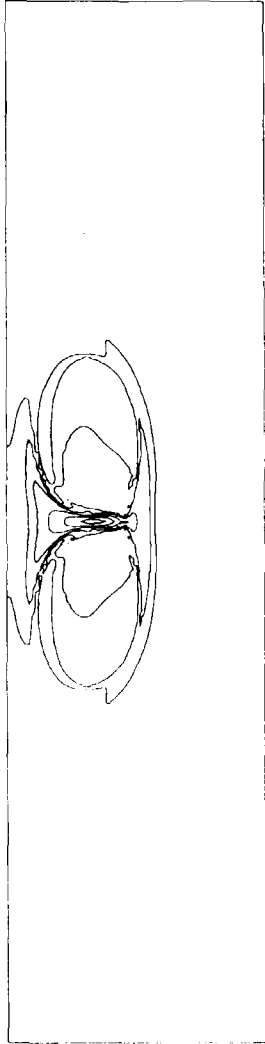
t = 0.00



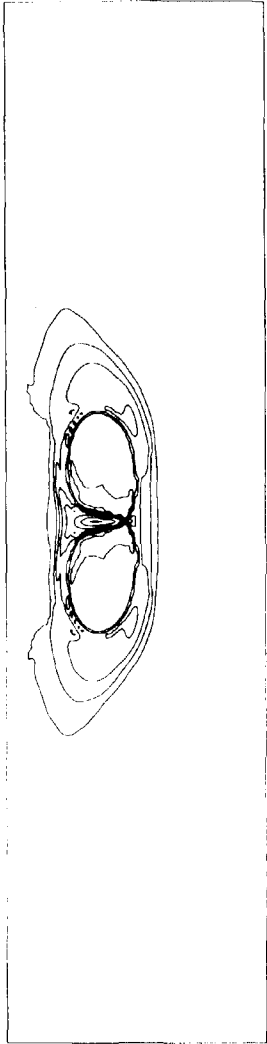
t = 5.00



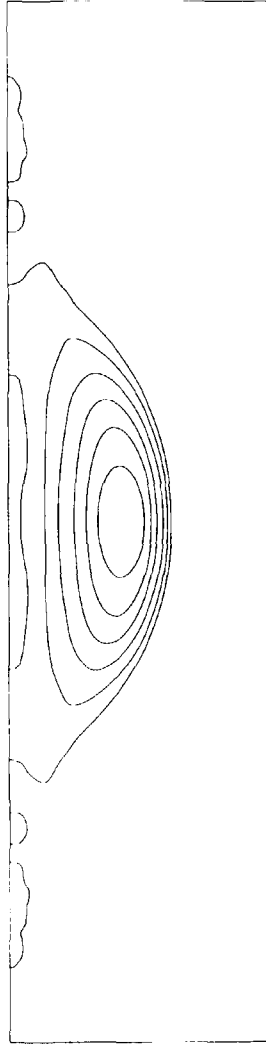
t = 10.00



t = 15.00



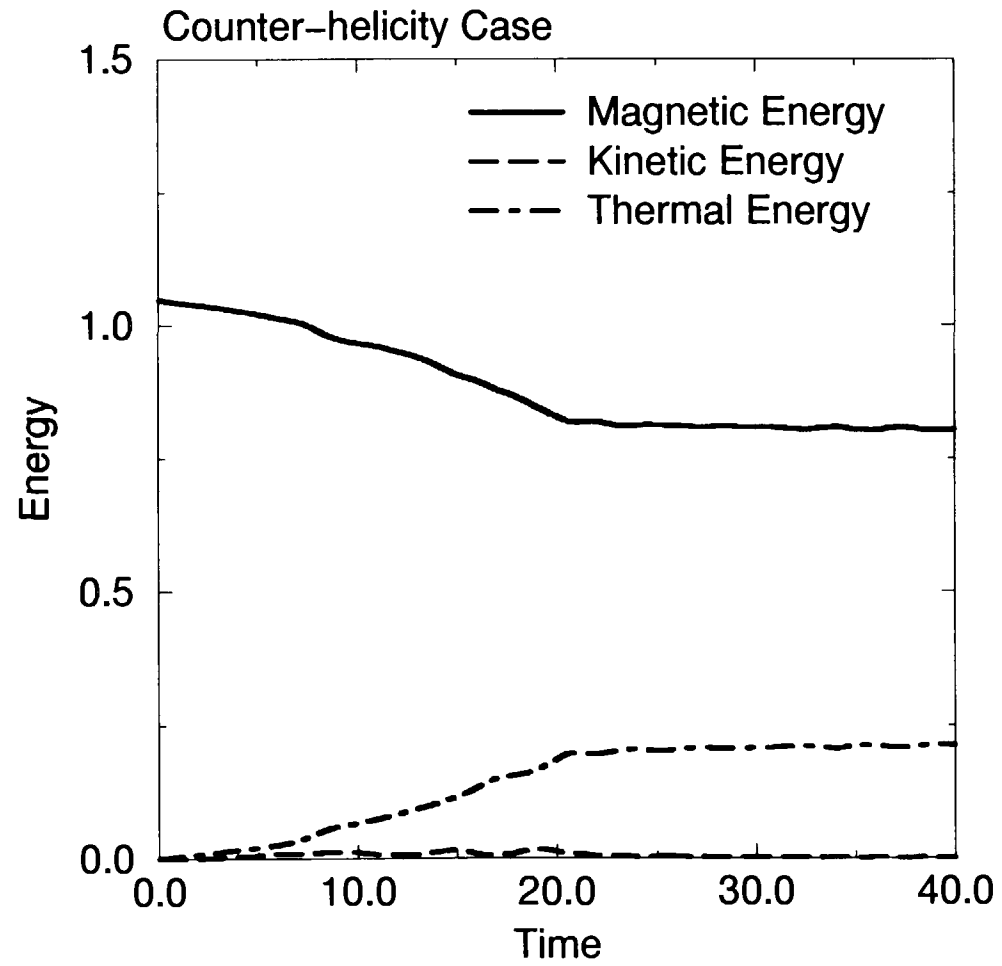
t = 40.00



Wat anabe

FIG.4

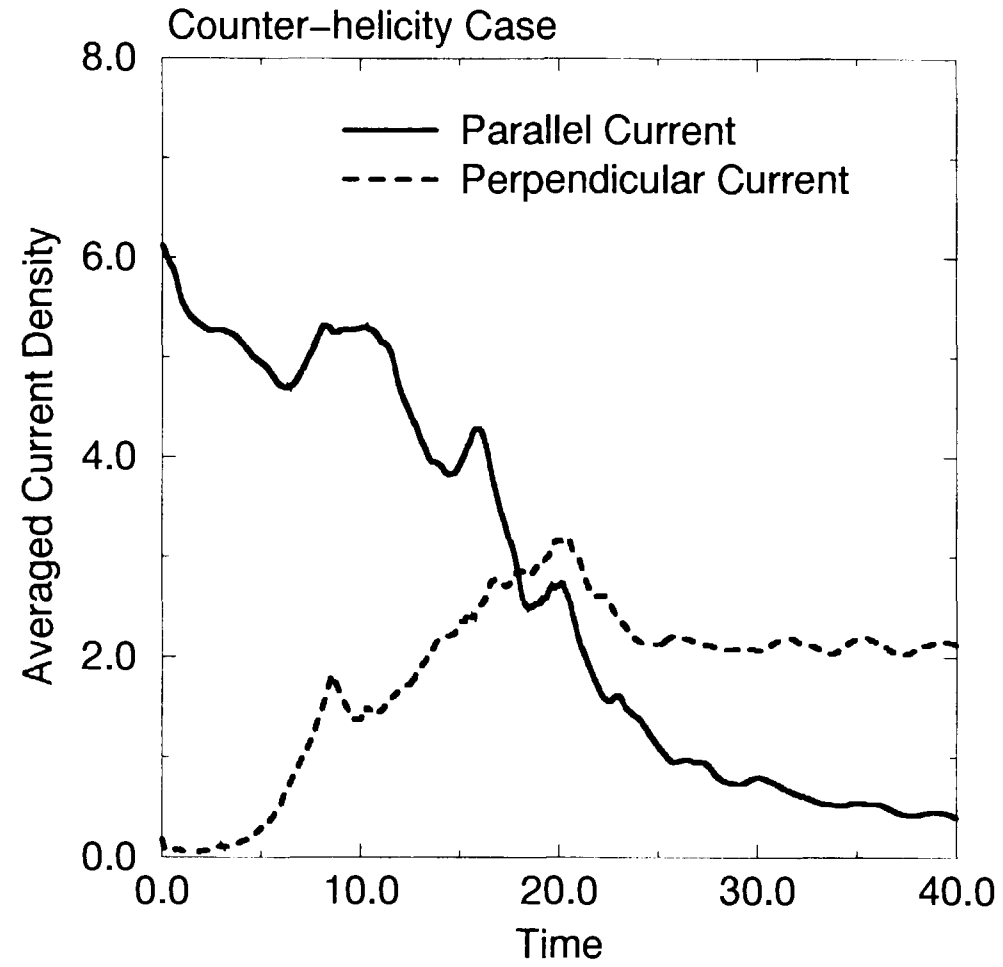
(a)



Watanabe

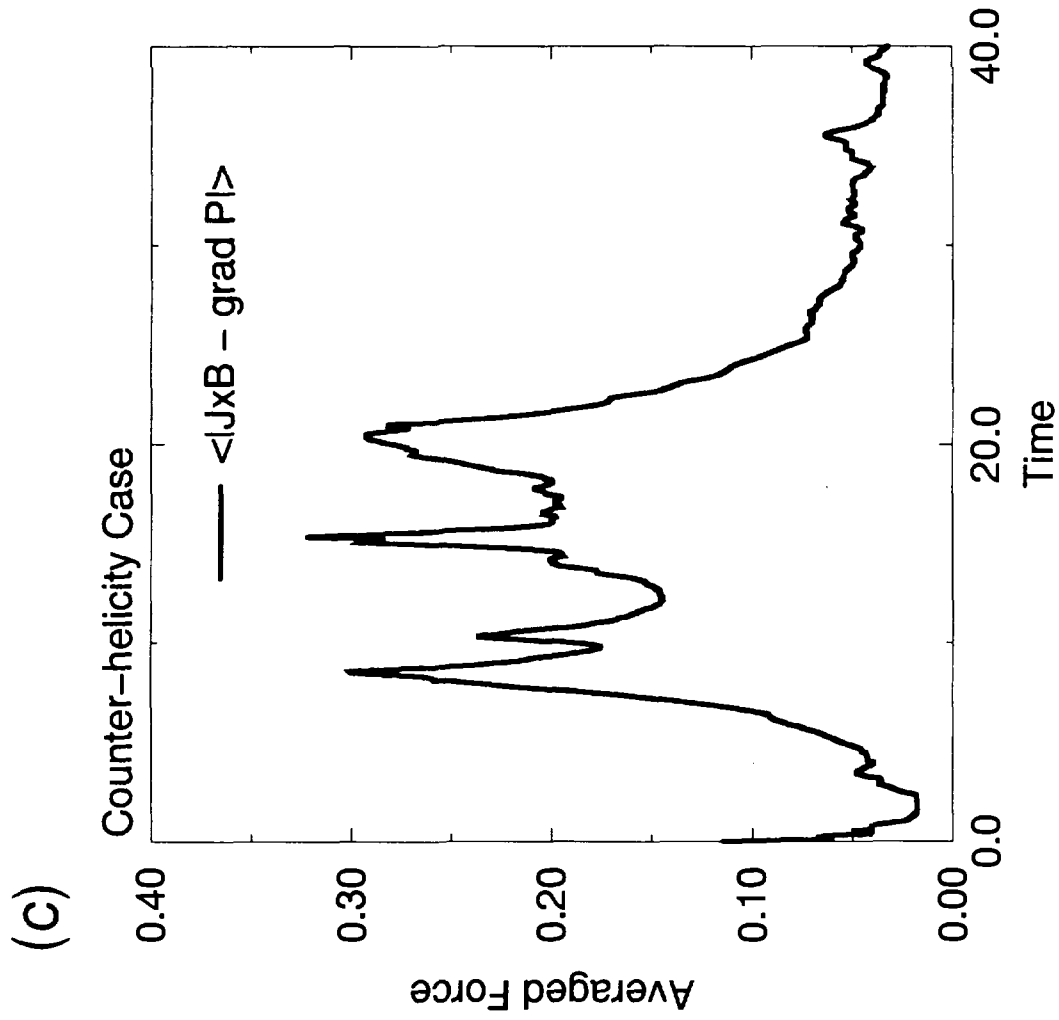
FIG.5 (a)

(b)



Watanabe

FIG.5 (b)

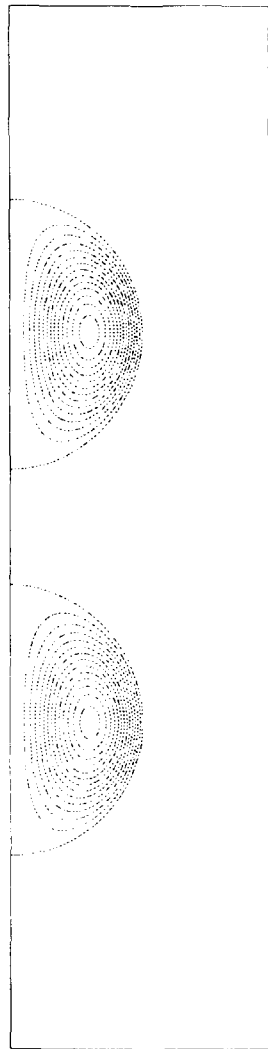


Watanabe

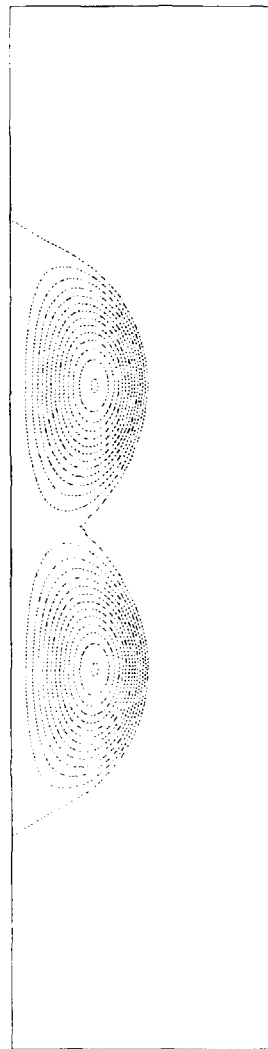
FIG.5 (c)

# Poloidal Flux (Co-helicity Case)

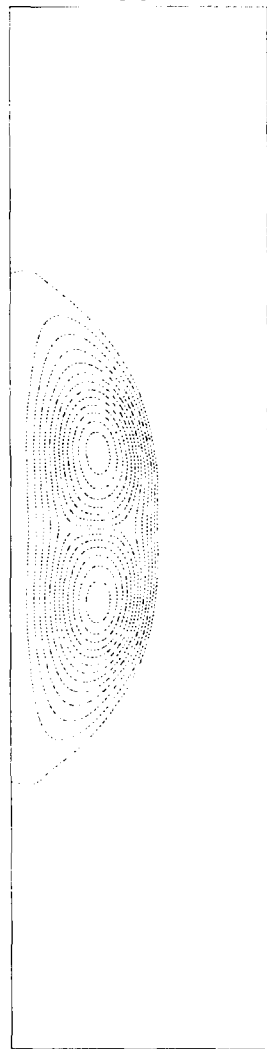
t = 0.00



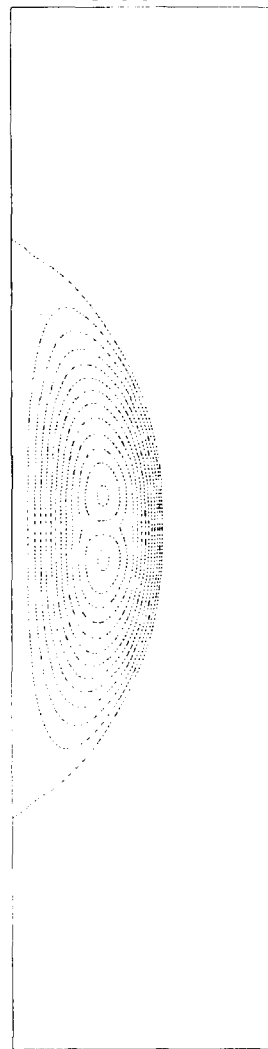
t = 5.00



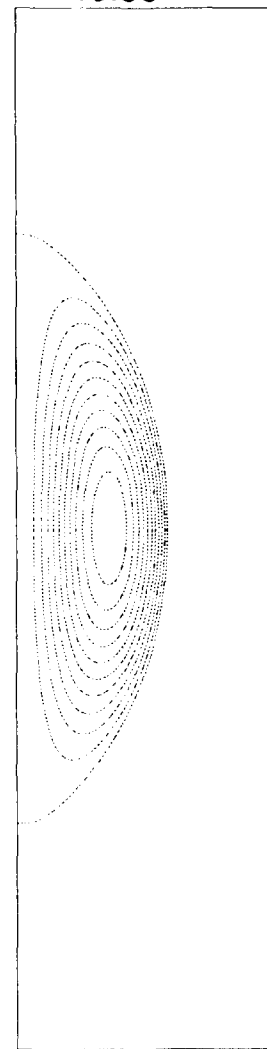
t = 10.00



t = 15.00



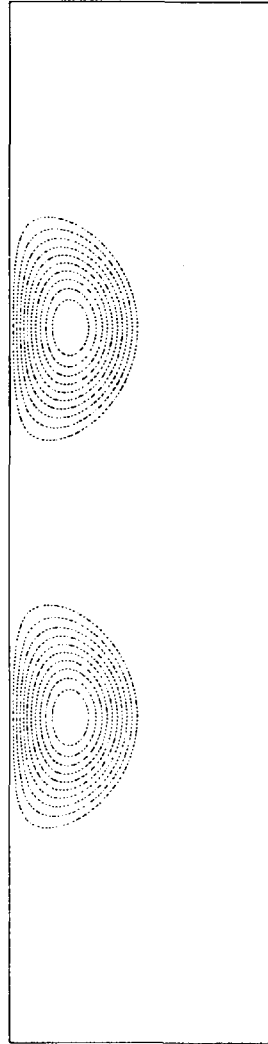
t = 40.00



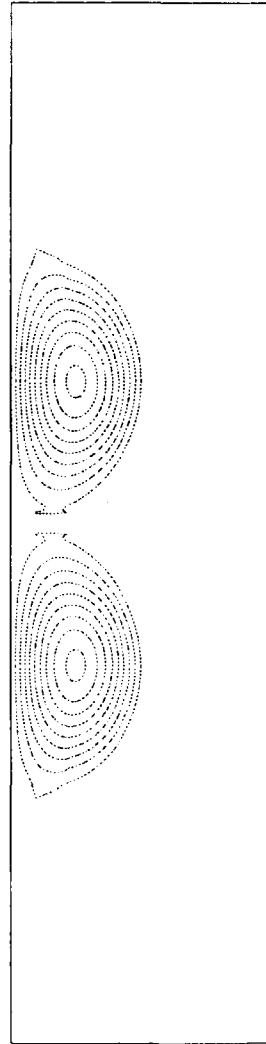
Wat anabe  
FIG.6

# Toroidal Field (Co-helicity Case)

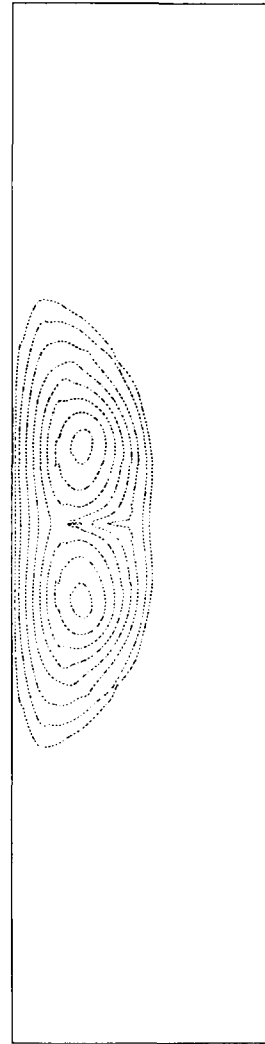
t = 0.00



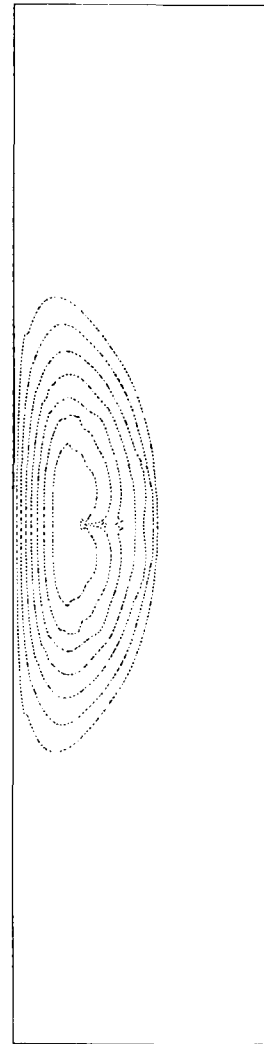
t = 5.00



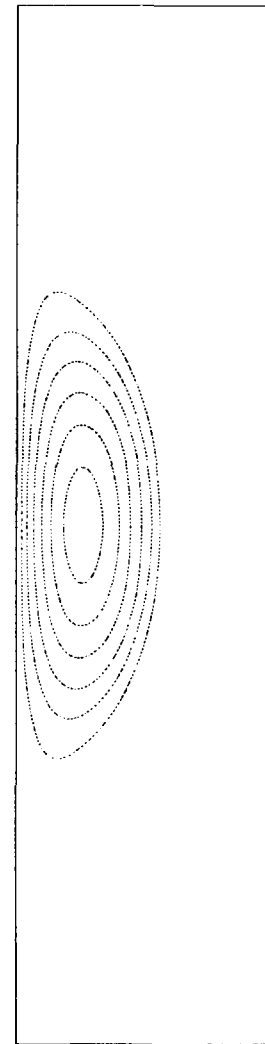
t = 10.00



t = 15.00



t = 40.00

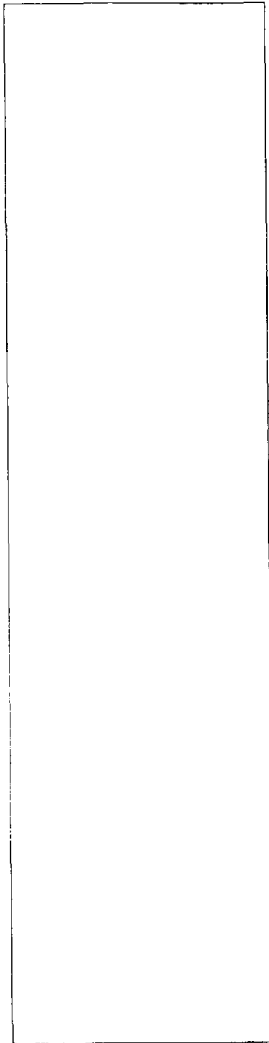


Wat anabe

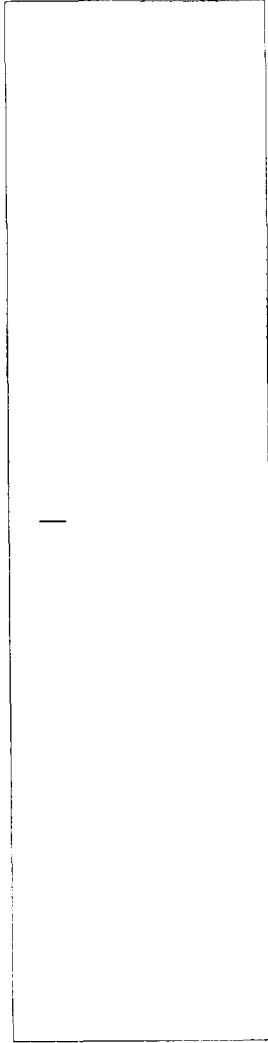
FIG.7

Pressure (Co-helicity Case)

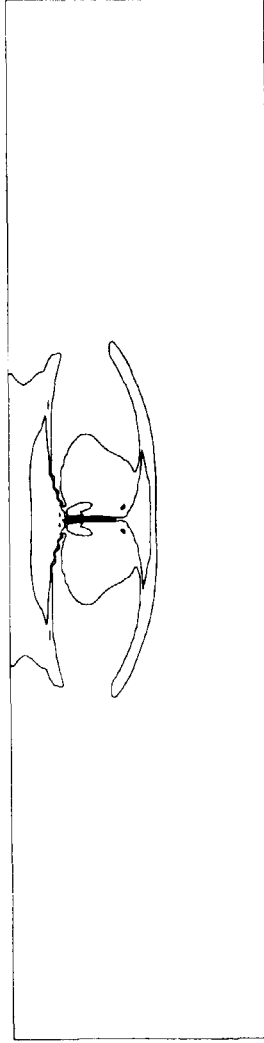
t = 0.00



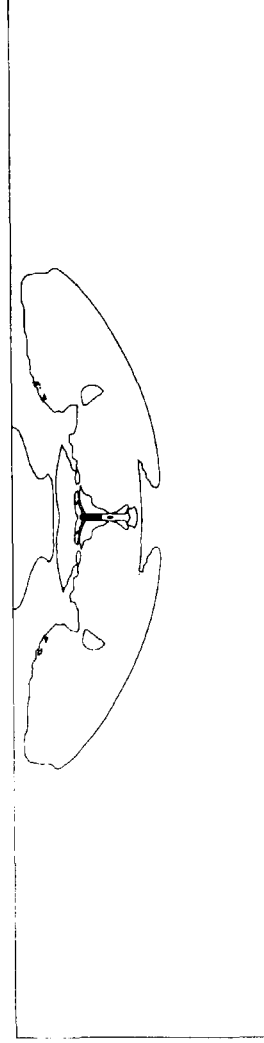
t = 5.00



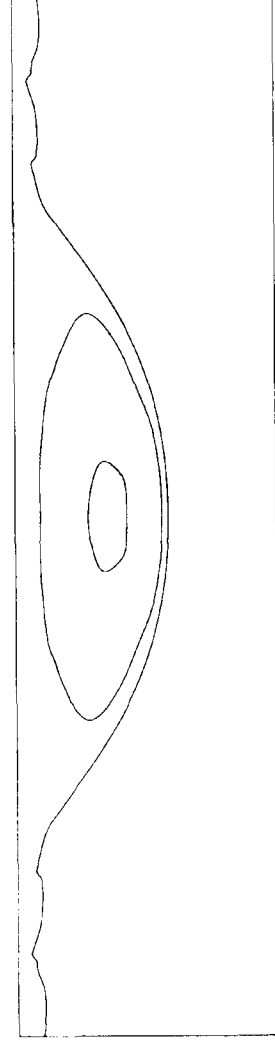
t = 10.00



t = 15.00



t = 40.00

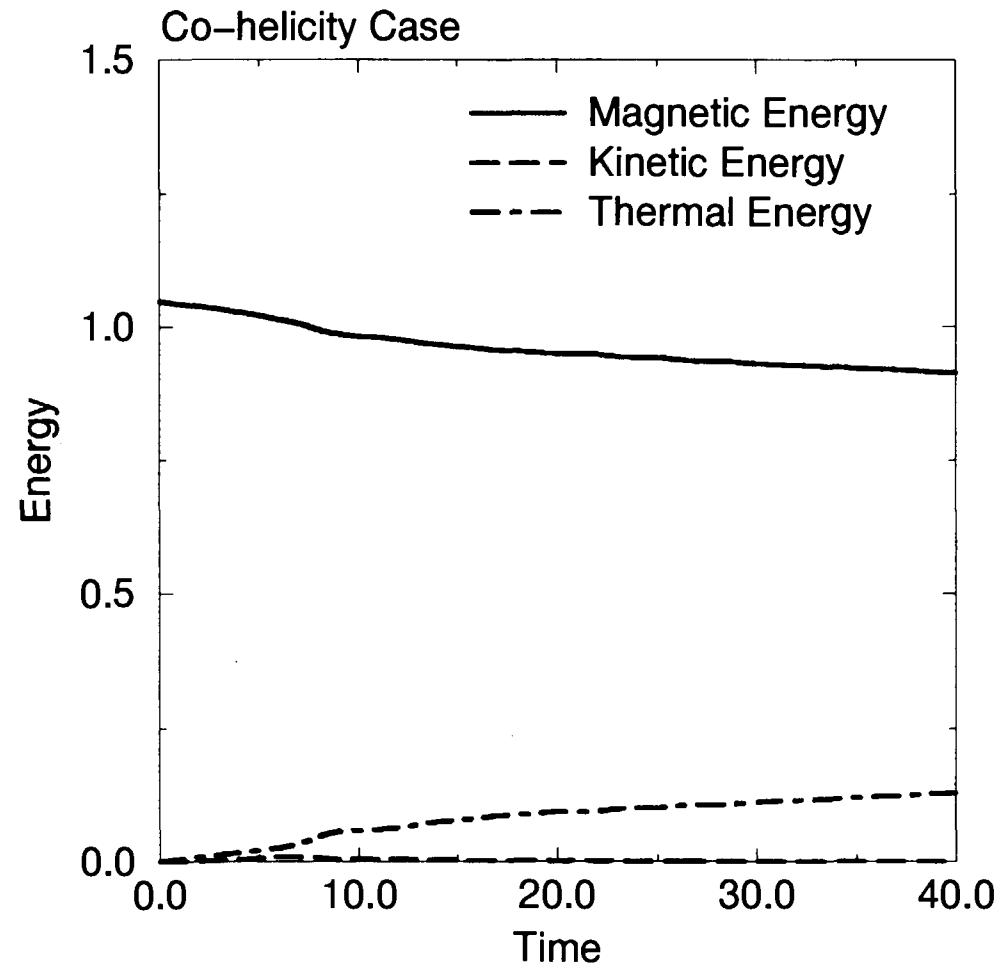


Watanabe

FIG.8



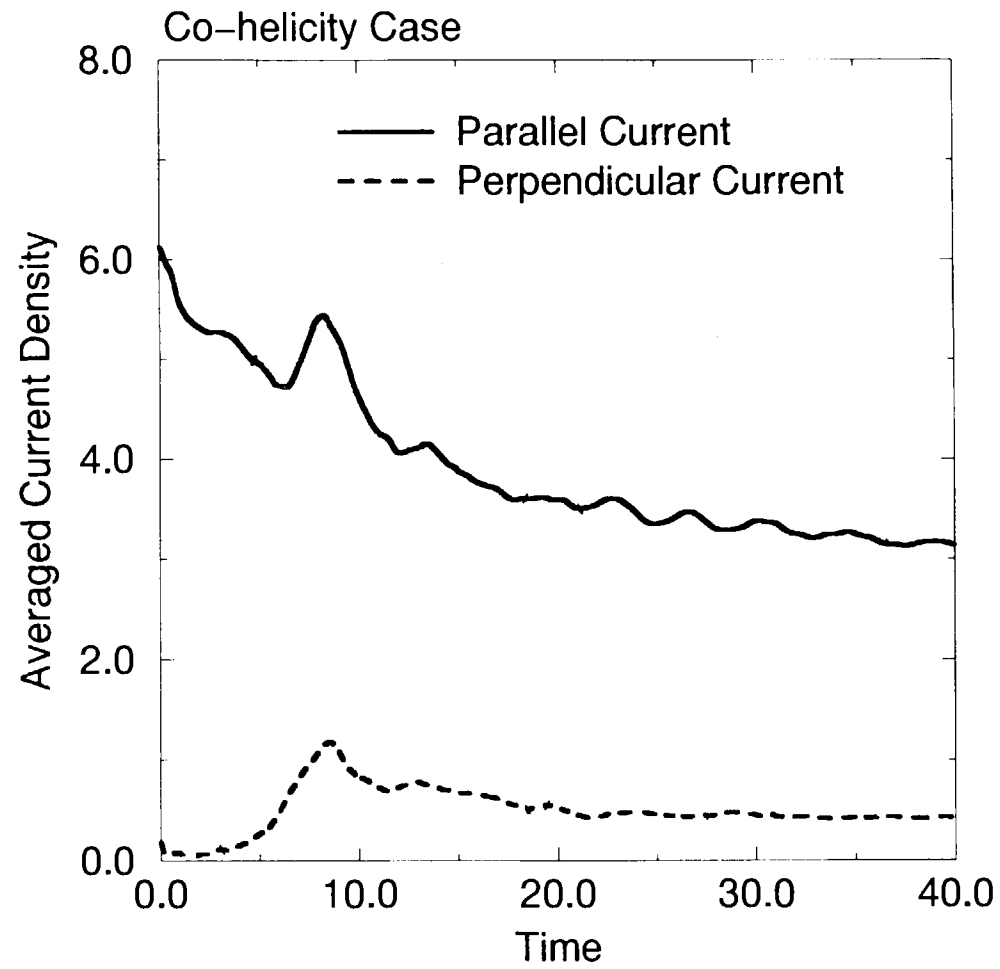
(a)



Wat anabe

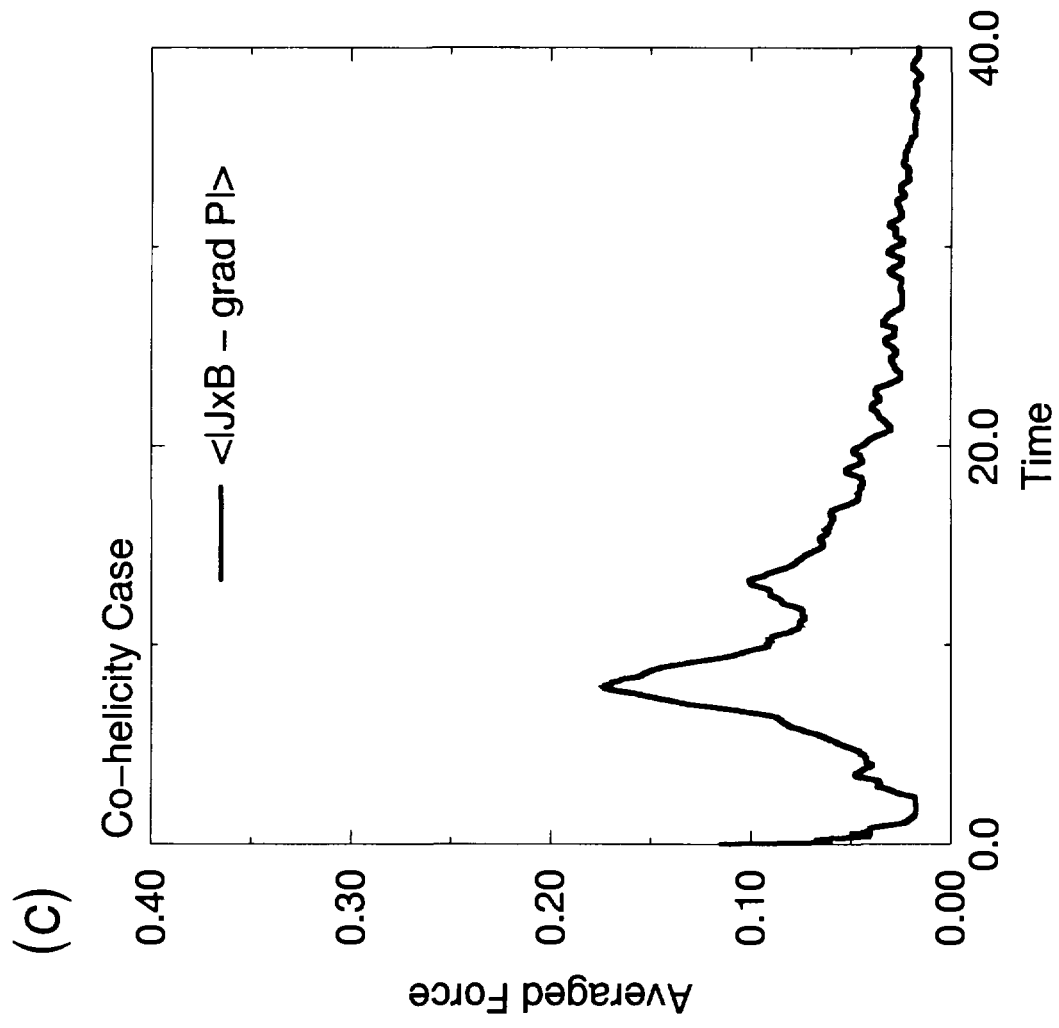
FIG.9 (a)

(b)



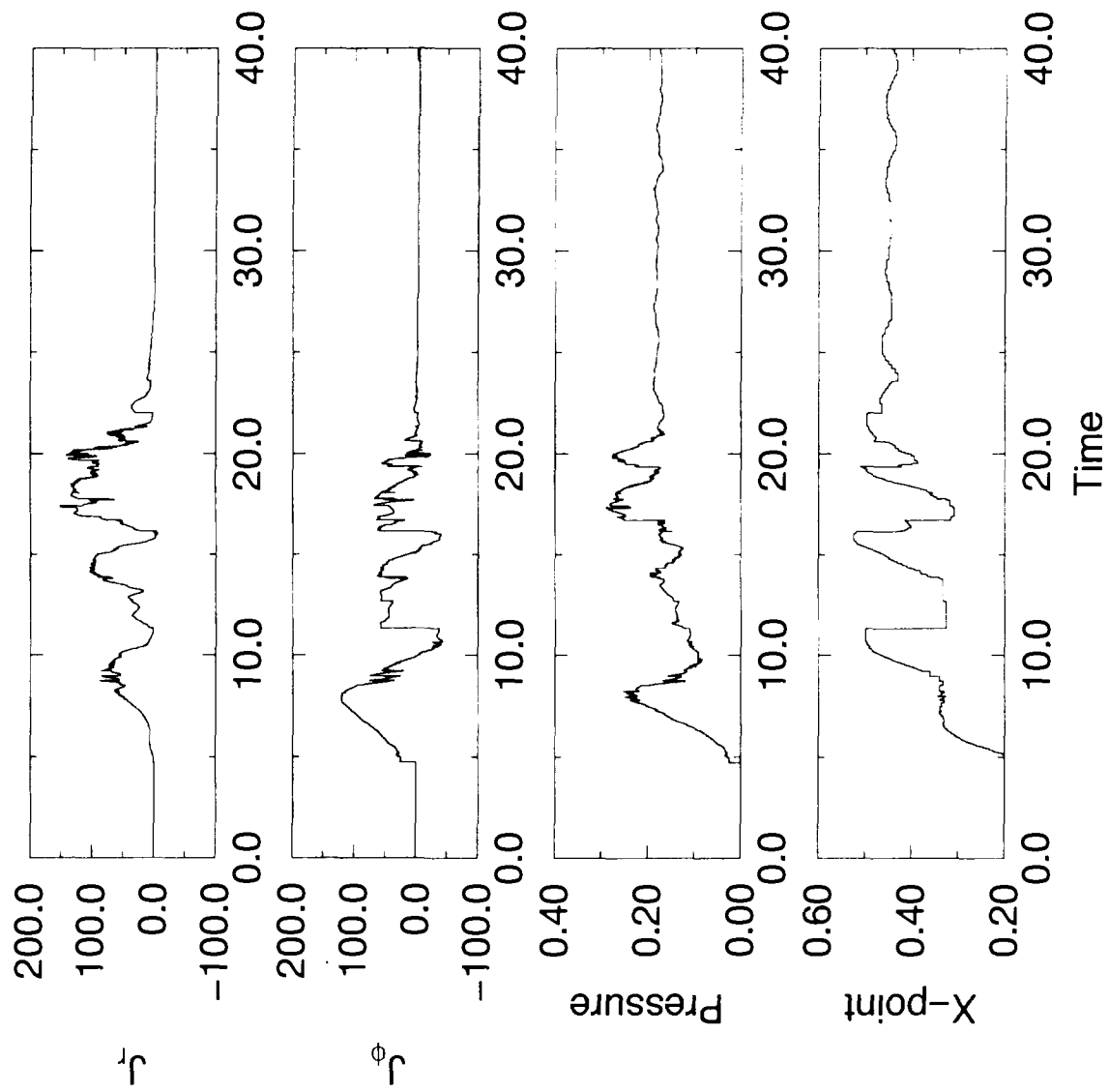
Wat anabe

FIG.9 (b)



Watanabe

FIG.9 (c)

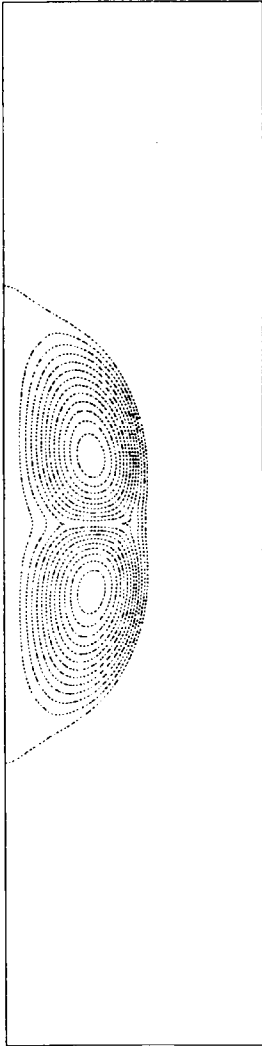


Watanabe

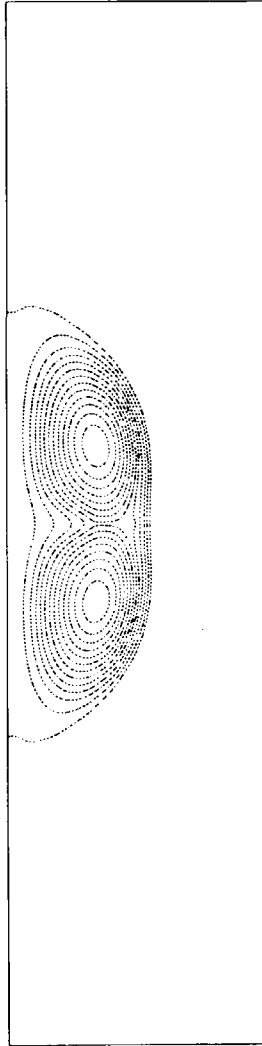
FIG.10

# Poloidal Flux (Counter-helicity Case)

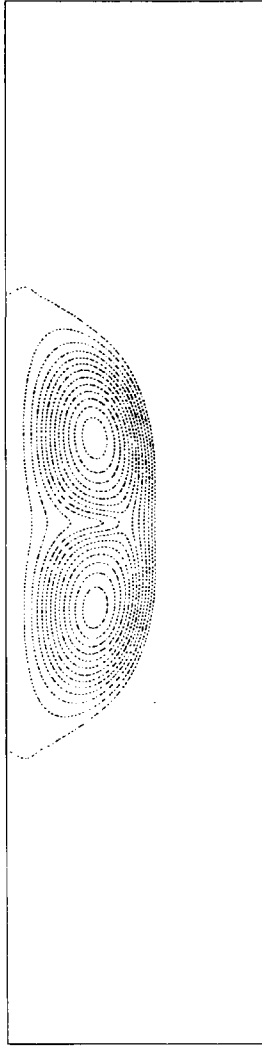
t = 8.00



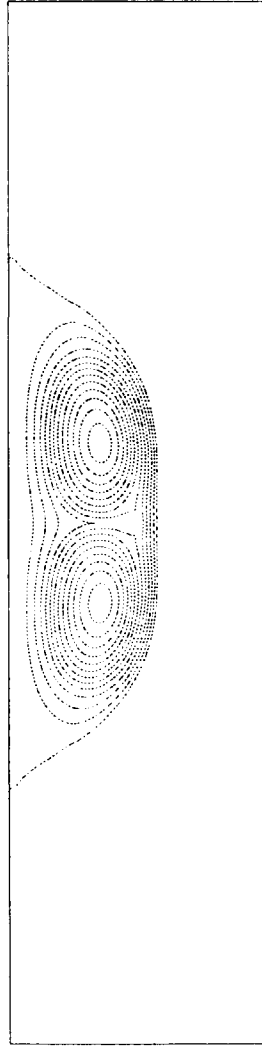
t = 9.00



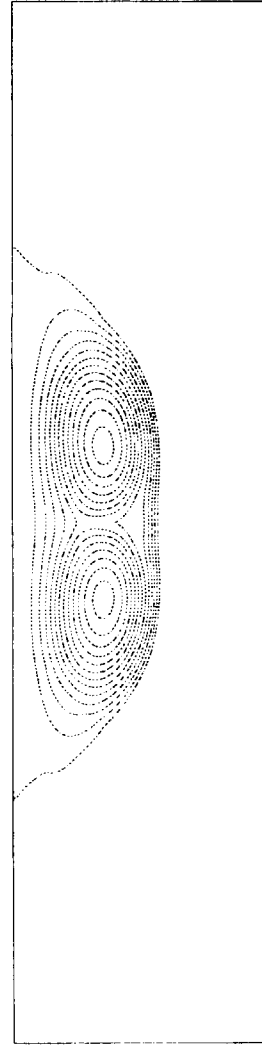
t = 10.00



t = 11.00

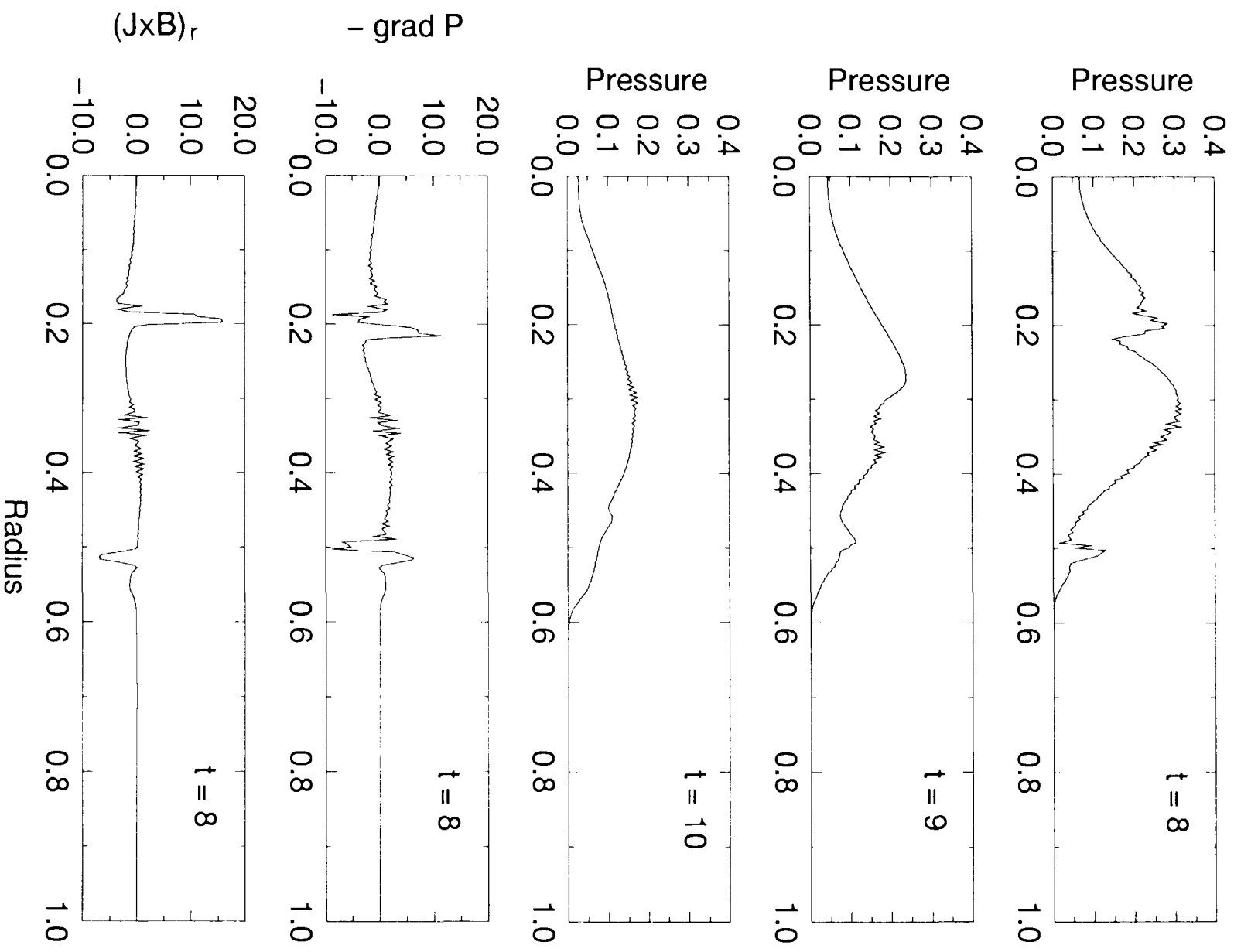


t = 12.00



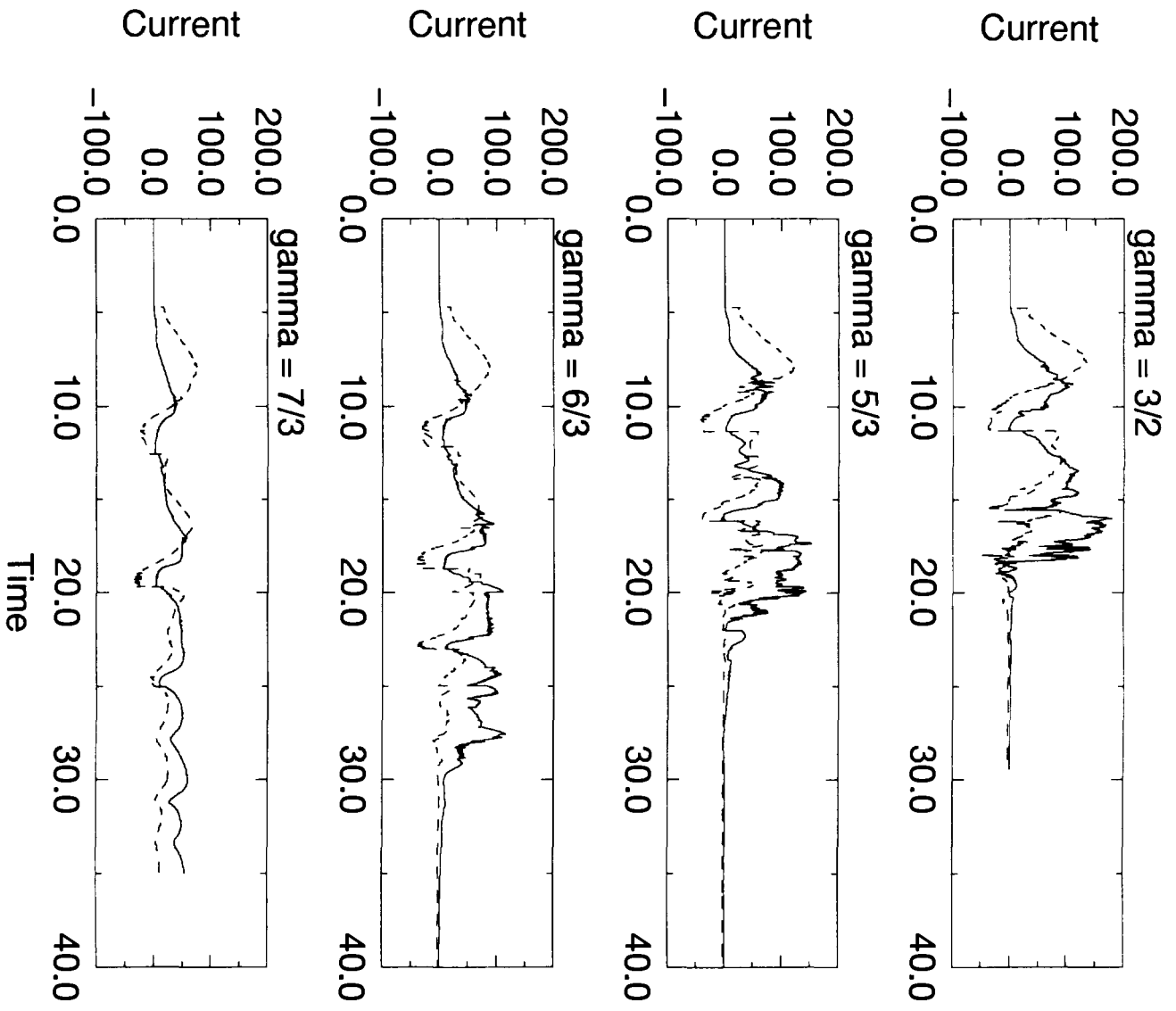
Watanabe

FIG.11

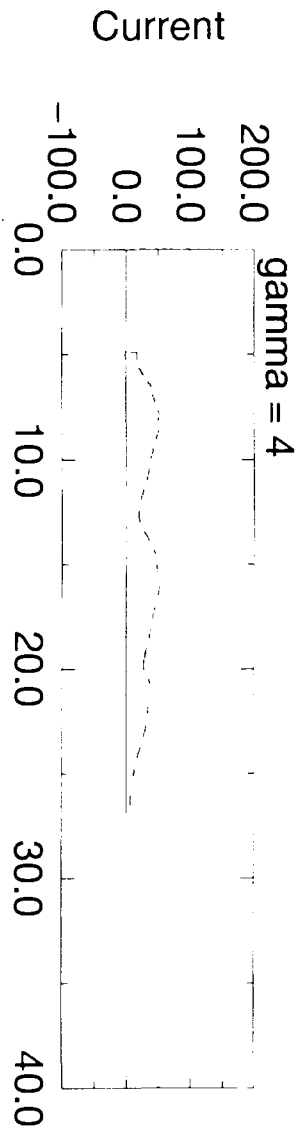
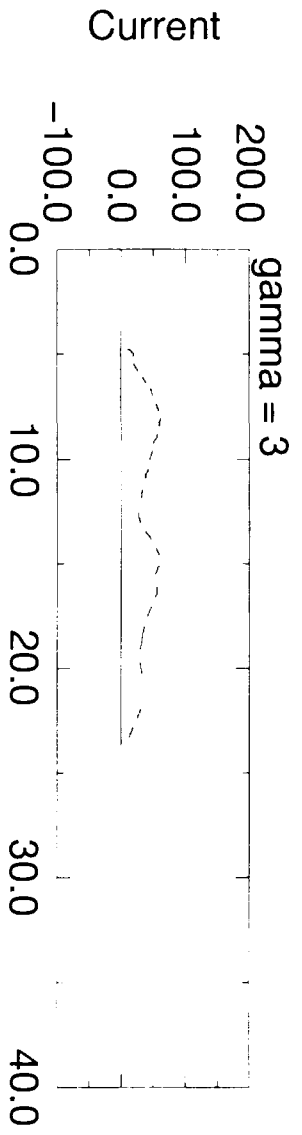
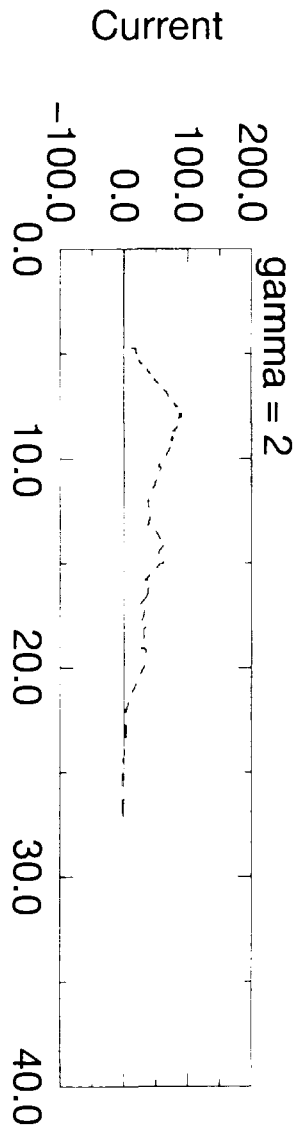
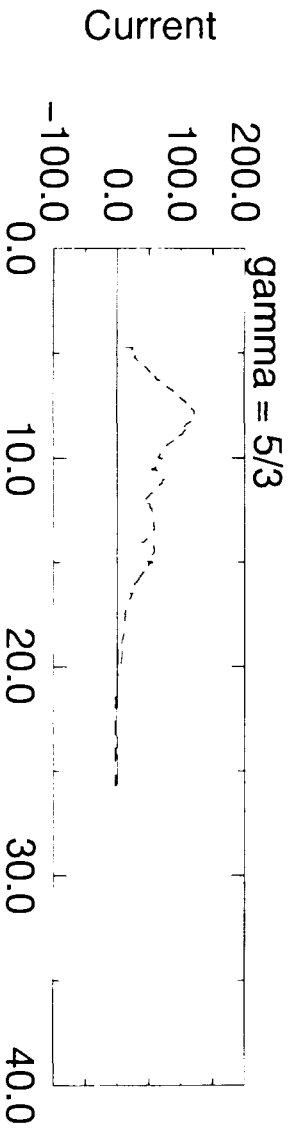


Watanabe

FIG.12

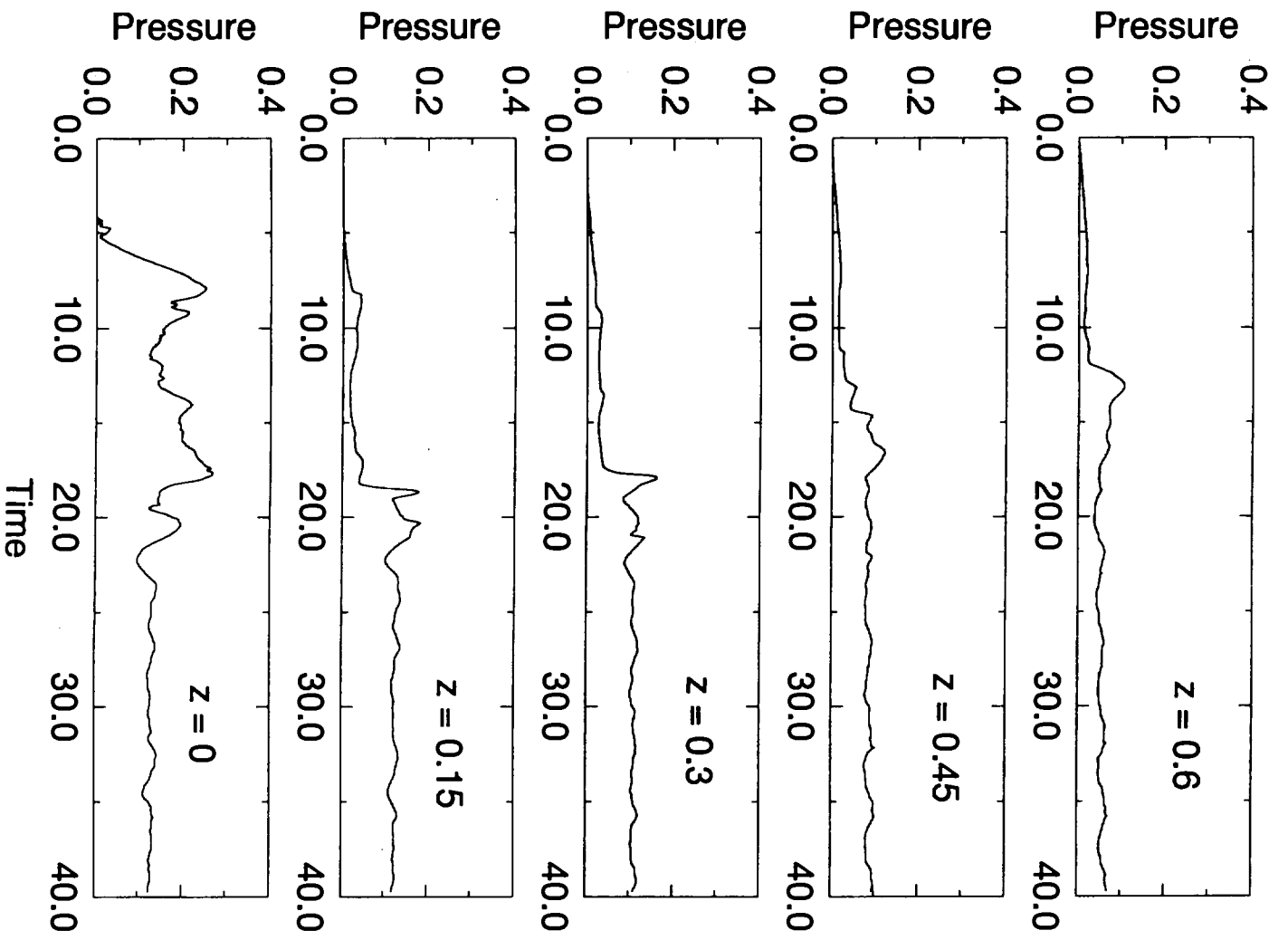


Wat anabe  
FIG.13



Wat anabe  
FIG. 14



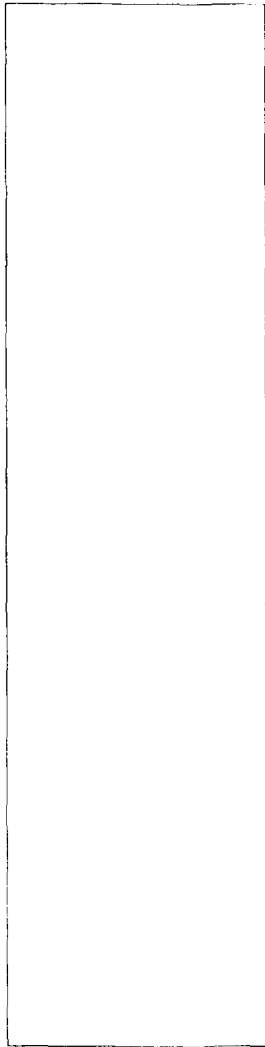


Watanabe

FIG.15

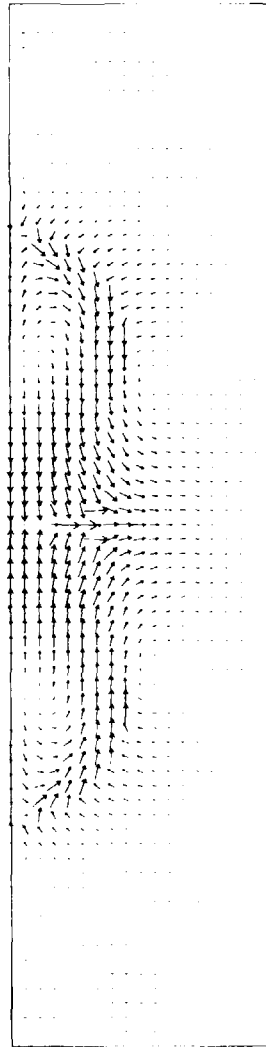
# Poloidal Flow (Counter-helicity Case)

t = 0.00



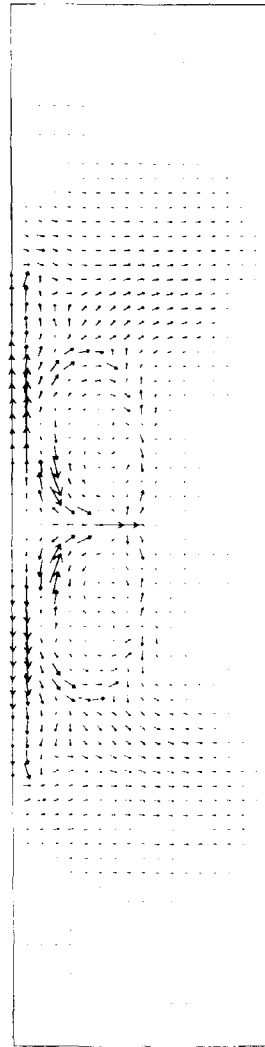
→: 0.25

t = 5.00



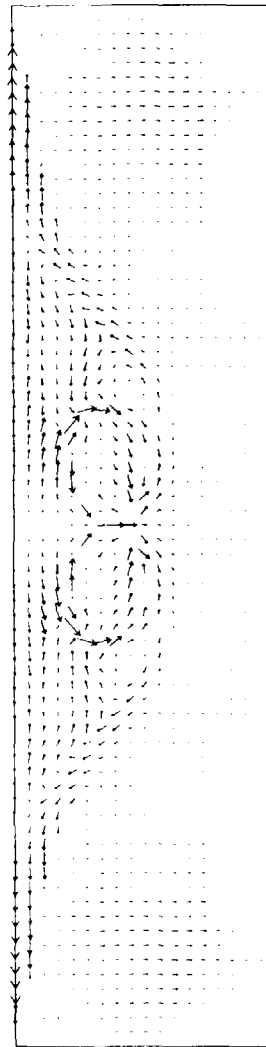
→: 0.25

t = 10.00



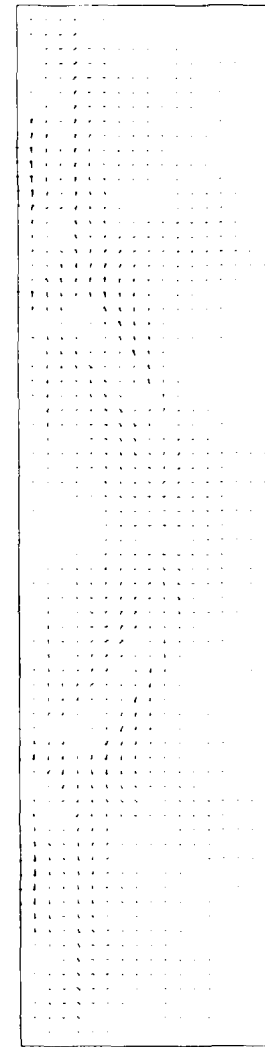
→: 0.25

t = 15.00



→: 0.25

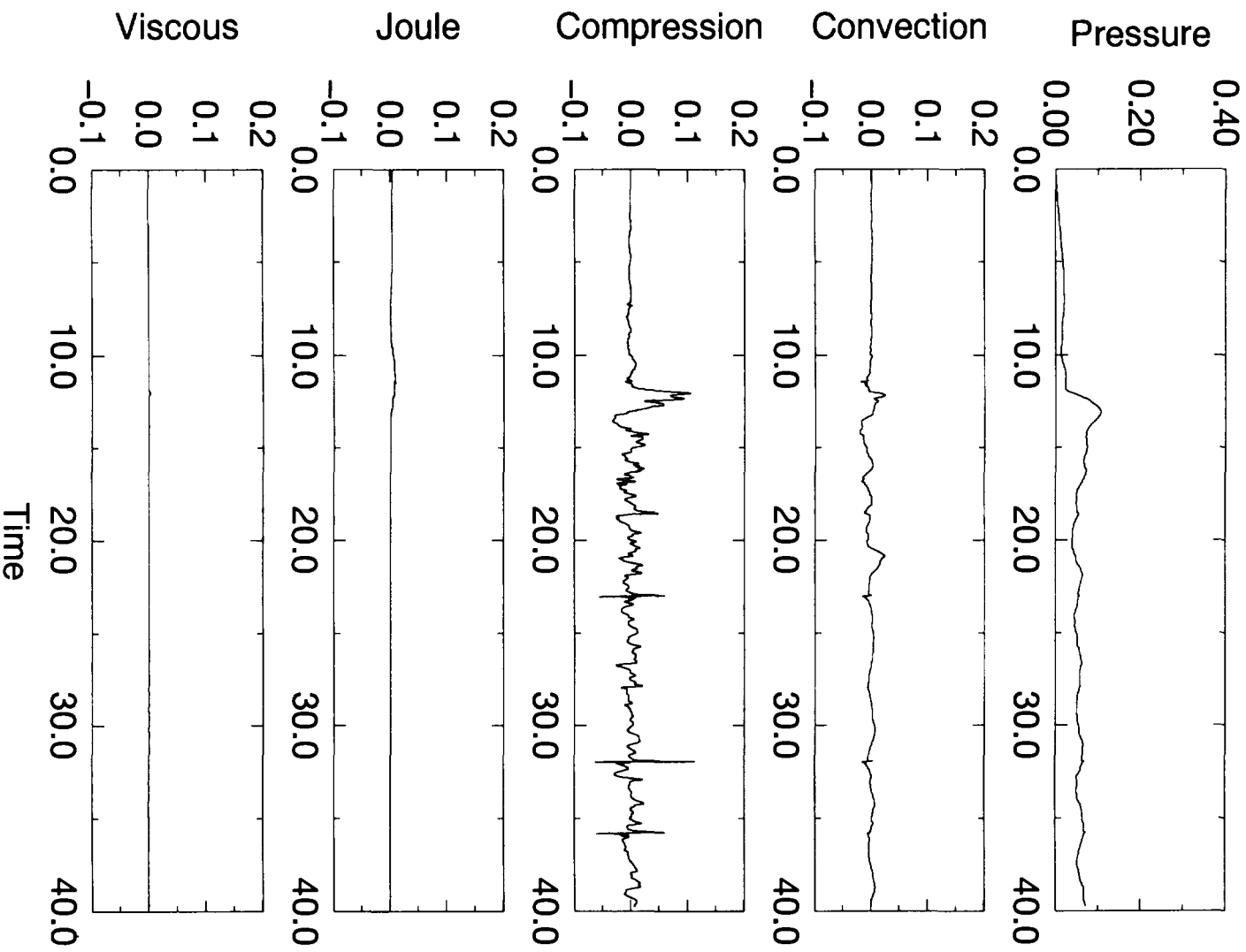
t = 40.00



→: 0.25

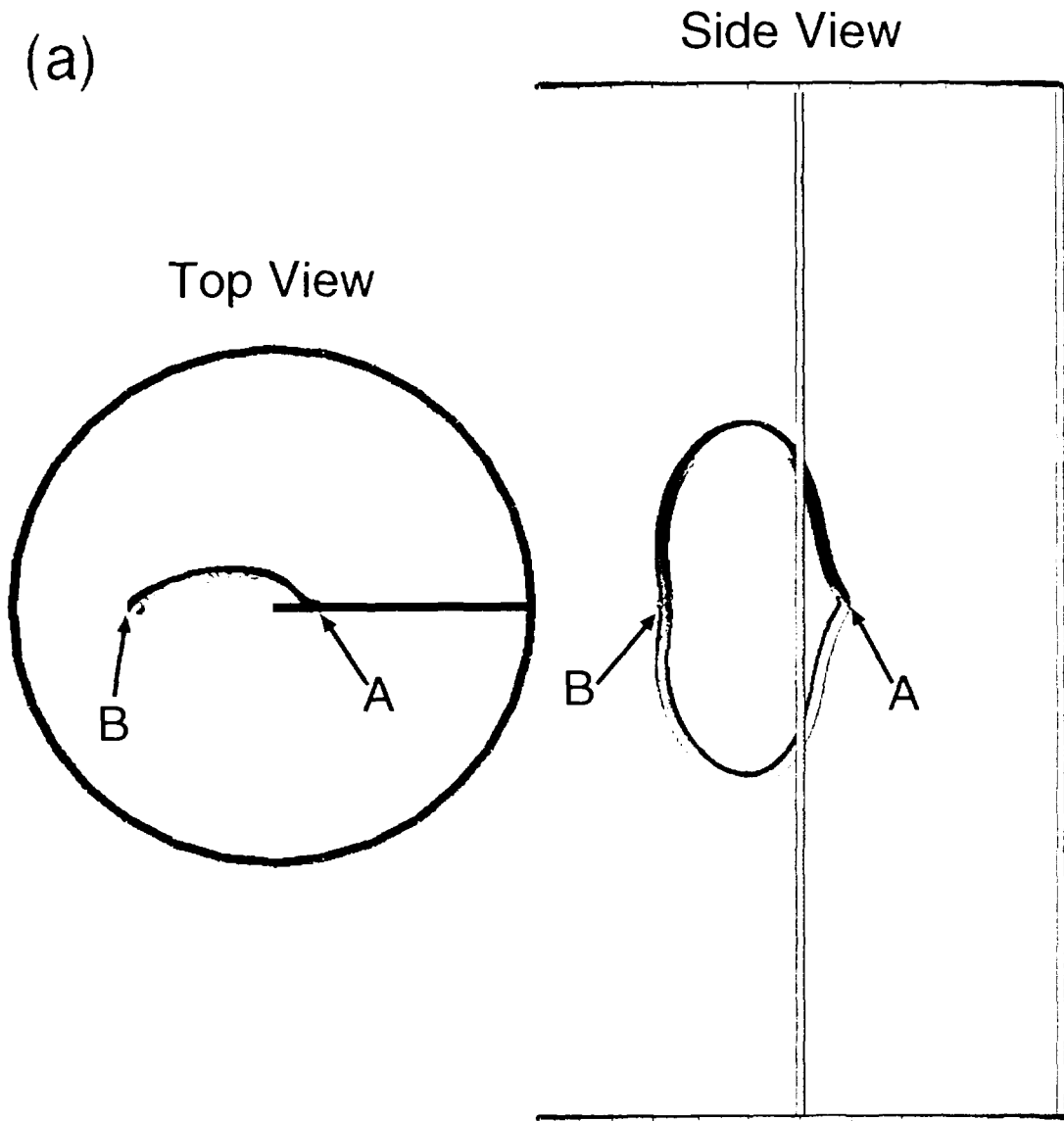
Wat anabe  
FIG.16

at  $(r,z) = (0.3,0.6)$



Wat anabe  
FIG.17

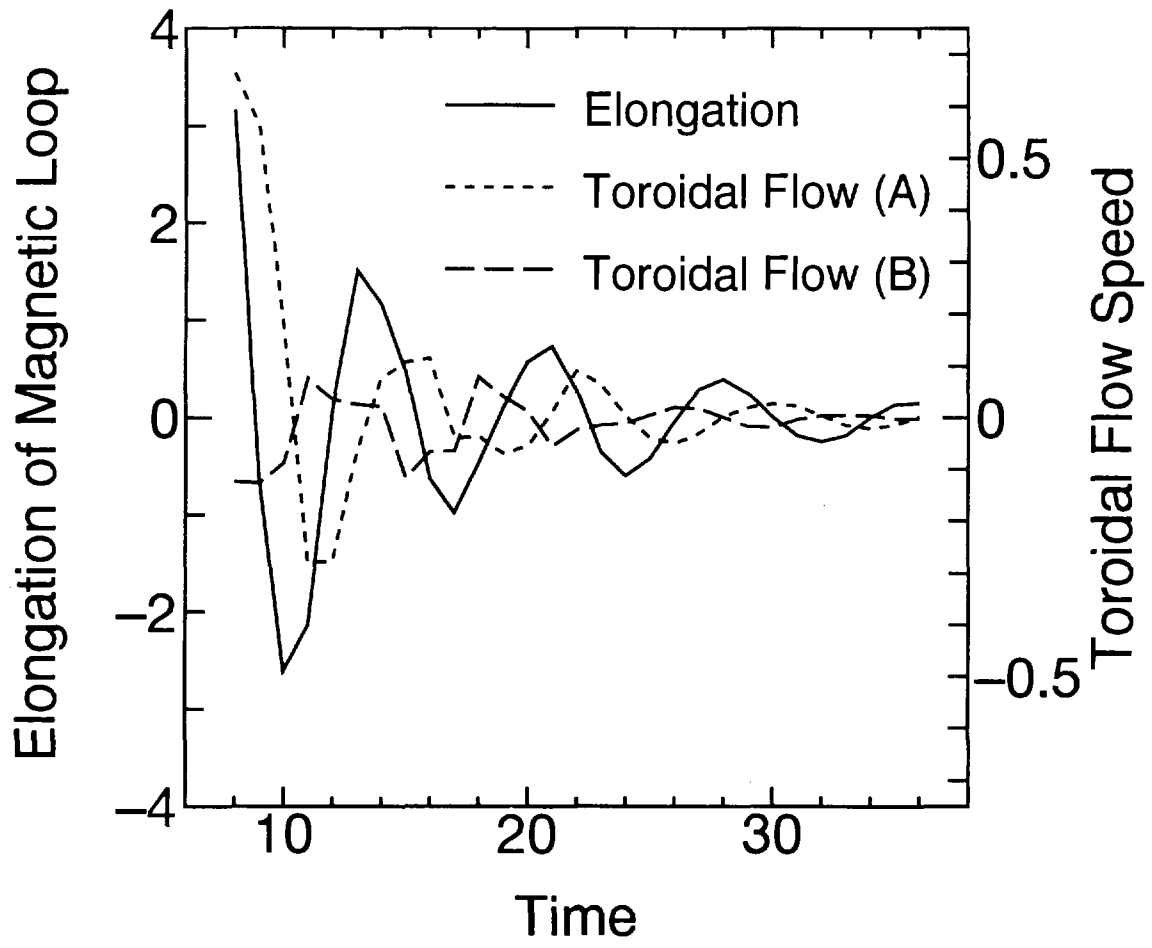
(a)



Wat anabe

FIG.18(a)

(b)



Wat anabe  
FIG.18(b)

## Recent Issues of NIFS Series

- NIFS-387 K. Araki, S. Yanase and J. Mizushima,  
*Symmetry Breaking by Differential Rotation and Saddle-node Bifurcation of the Thermal Convection in a Spherical Shell*; Dec. 1995
- NIFS-388 V.D. Pustovitov,  
*Control of Pfirsch-Schlüter Current by External Poloidal Magnetic Field in Conventional Stellarators*; Dec. 1995
- NIFS-389 K. Akaishi,  
*On the Outgassing Rate Versus Time Characteristics in the Pump-down of an Unbaked Vacuum System*; Dec. 1995
- NIFS-390 K.N. Sato, S. Murakami, N. Nakajima, K. Itoh,  
*Possibility of Simulation Experiments for Fast Particle Physics in Large Helical Device (LHD)*; Dec. 1995
- NIFS-391 W.X.Wang, M. Okamoto, N. Nakajima, S. Murakami and N. Ohyaabu,  
*A Monte Carlo Simulation Model for the Steady-State Plasma in the Scrape-off Layer*; Dec. 1995
- NIFS-392 Shao-ping Zhu, R. Horiuchi, T. Sato and The Complexity Simulation Group,  
*Self-organization Process of a Magnetohydrodynamic Plasma in the Presence of Thermal Conduction*; Dec. 1995
- NIFS-393 M. Ozaki, T. Sato, R. Horiuchi and the Complexity Simulation Group  
*Electromagnetic Instability and Anomalous Resistivity in a Magnetic Neutral Sheet*; Dec. 1995
- NIFS-394 K. Itoh, S.-I Itoh, M. Yagi and A. Fukuyama,  
*Subcritical Excitation of Plasma Turbulence*; Jan. 1996
- NIFS-395 H. Sugama and M. Okamoto, W. Horton and M. Wakatani,  
*Transport Processes and Entropy Production in Toroidal Plasmas with Gyrokinetic Electromagnetic Turbulence*; Jan. 1996
- NIFS-396 T. Kato, T. Fujiwara and Y. Hanaoka,  
*X-ray Spectral Analysis of Yohkoh BCS Data on Sep. 6 1992 Flares - Blue Shift Component and Ion Abundances -*; Feb. 1996
- NIFS-397 H. Kuramoto, N. Hiraki, S. Moriyama, K. Toi, K. Sato, K. Narihara, A. Ejiri, T. Seki and JIPP T-IIU Group,  
*Measurement of the Poloidal Magnetic Field Profile with High Time Resolution Zeeman Polarimeter in the JIPP T-IIU Tokamak*; Feb. 1996
- NIFS-398 J.F. Wang, T. Amano, Y. Ogawa, N. Inoue,  
*Simulation of Burning Plasma Dynamics in ITER*; Feb. 1996

- NIFS-399 K. Itoh, S-I. Itoh, A. Fukuyama and M. Yagi,  
*Theory of Self-Sustained Turbulence in Confined Plasmas*; Feb. 1996
- NIFS-400 J. Uramoto,  
*A Detection Method of Negative Pionlike Particles from a H<sub>2</sub> Gas Discharge Plasma*; Feb. 1996
- NIFS-401 K. Ida, J. Xu, K.N. Sato, H. Sakakita and JIPP TII-U group,  
*Fast Charge Exchange Spectroscopy Using a Fabry-Perot Spectrometer in the JIPP TII-U Tokamak*; Feb. 1996
- NIFS-402 T. Amano,  
*Passive Shut-Down of ITER Plasma by Be Evaporation*; Feb. 1996
- NIFS-403 K. Orito,  
*A New Variable Transformation Technique for the Nonlinear Drift Vortex*; Feb. 1996
- NIFS-404 T. Oike, K. Kitachi, S. Ohdachi, K. Toi, S. Sakakibara, S. Morita, T. Morisaki, H. Suzuki, S. Okamura, K. Matsuoka and CHS group; *Measurement of Magnetic Field Fluctuations near Plasma Edge with Movable Magnetic Probe Array in the CHS Heliotron/Torsatron*; Mar. 1996
- NIFS-405 S.K. Guharay, K. Tsumori, M. Hamabe, Y. Takeiri, O. Kaneko, T. Kuroda,  
*Simple Emittance Measurement of H<sup>-</sup> Beams from a Large Plasma Source*; Mar. 1996
- NIFS-406 M. Tanaka and D. Biskamp,  
*Symmetry-Breaking due to Parallel Electron Motion and Resultant Scaling in Collisionless Magnetic Reconnection*; Mar. 1996
- NIFS-407 K. Kitachi, T. Oike, S. Ohdachi, K. Toi, R. Akiyama, A. Ejiri, Y. Hamada, H. Kuramoto, K. Narihara, T. Seki and JIPP T-IIU Group,  
*Measurement of Magnetic Field Fluctuations within Last Closed Flux Surface with Movable Magnetic Probe Array in the JIPP T-IIU Tokamak*; Mar. 1996
- NIFS-408 K. Hirose, S. Saito and Yoshi.H. Ichikawa  
*Structure of Period-2 Step-1 Accelerator Island in Area Preserving Maps*; Mar. 1996
- NIFS-409 G.Y. Yu, M. Okamoto, H. Sanuki, T. Amano,  
*Effect of Plasma Inertia on Vertical Displacement Instability in Tokamaks*; Mar. 1996
- NIFS-410 T. Yamagishi,  
*Solution of Initial Value Problem of Gyro-Kinetic Equation*; Mar. 1996

- NIFS-411 K. Ida and N. Nakajima,  
*Comparison of Parallel Viscosity with Neoclassical Theory*; Apr. 1996
- NIFS-412 T. Ohkawa and H. Ohkawa,  
*Cuspher, A Combined Confinement System*; Apr. 1996
- NIFS-413 Y. Nomura, Y.H. Ichikawa and A.T. Filippov,  
*Stochasticity in the Josephson Map*; Apr. 1996
- NIFS-414 J. Uramoto,  
*Production Mechanism of Negative Pionlike Particles in H<sub>2</sub> Gas Discharge Plasma*; Apr. 1996
- NIFS-415 A. Fujisawa, H. Iguchi, S. Lee, T.P. Crowley, Y. Hamada, S. Hidekuma, M. Kojima,  
*Active Trajectory Control for a Heavy Ion Beam Probe on the Compact Helical System*; May 1996
- NIFS-416 M. Iwase, K. Ohkubo, S. Kubo and H. Idei  
*Band Rejection Filter for Measurement of Electron Cyclotron Emission during Electron Cyclotron Heating*; May 1996
- NIFS-417 T. Yabe, H. Daido, T. Aoki, E. Matsunaga and K. Arisawa,  
*Anomalous Crater Formation in Pulsed-Laser-Illuminated Aluminum Slab and Debris Distribution*; May 1996
- NIFS-418 J. Uramoto,  
*Extraction of K<sup>-</sup> Mesonlike Particles from a D<sub>2</sub> Gas Discharge Plasma in Magnetic Field*; May 1996
- NIFS-419 J. Xu, K. Toi, H. Kuramoto, A. Nishizawa, J. Fujita, A. Ejiri, K. Narihara, T. Seki, H. Sakakita, K. Kawahata, K. Ida, K. Adachi, R. Akiyama, Y. Hamada, S. Hirokura, Y. Kawasumi, M. Kojima, I. Nomura, S. Ohdachi, K.N. Sato  
*Measurement of Internal Magnetic Field with Motional Stark Polarimetry in Current Ramp-Up Experiments of JIPP T-IIU*; June 1996
- NIFS-420 Y.N. Nejoh,  
*Arbitrary Amplitude Ion-acoustic Waves in a Relativistic Electron-beam Plasma System*; July 1996
- NIFS-421 K. Kondo, K. Ida, C. Christou, V.Yu.Sergeev, K.V.Khlopenkov, S.Sudo, F. Sano, H. Zushi, T. Mizuuchi, S. Besshou, H. Okada, K. Nagasaki, K. Sakamoto, Y. Kurimoto, H. Funaba, T. Hamada, T. Kinoshita, S. Kado, Y. Kanda, T. Okamoto, M. Wakatani and T. Obiki,  
*Behavior of Pellet Injected Li Ions into Heliotron E Plasmas*; July 1996
- NIFS-422 Y. Kondoh, M. Yamaguchi and K. Yokozuka,  
*Simulations of Toroidal Current Drive without External Magnetic Helicity*



*Injection; July 1996*

- NIFS-423 Joong-San Koog,  
*Development of an Imaging VUV Monochromator in Normal Incidence Region; July 1996*
- NIFS-424 K. Orito,  
*A New Technique Based on the Transformation of Variables for Nonlinear Drift and Rossby Vortices; July 1996*
- NIFS-425 A. Fujisawa, H. Iguchi, S. Lee, T.P. Crowley, Y. Hamada, H. Sanuki, K. Itoh, S. Kubo, H. Idei, T. Minami, K. Tanaka, K. Ida, S. Nishimura, S. Hidekuma, M. Kojima, C. Takahashi, S. Okamura and K. Matsuoka,  
*Direct Observation of Potential Profiles with a 200keV Heavy Ion Beam Probe and Evaluation of Loss Cone Structure in Toroidal Helical Plasmas on the Compact Helical System; July 1996*
- NIFS-426 H. Kitauchi, K. Araki and S. Kida,  
*Flow Structure of Thermal Convection in a Rotating Spherical Shell; July 1996*
- NIFS-427 S. Kida and S. Goto,  
*Lagrangian Direct-interaction Approximation for Homogeneous Isotropic Turbulence; July 1996*
- NIFS-428 V.Yu. Sergeev, K.V. Khlopenkov, B.V. Kuteev, S. Sudo, K. Kondo, F. Sano, H. Zushi, H. Okada, S. Besshou, T. Mizuuchi, K. Nagasaki, Y. Kurimoto and T. Obiki,  
*Recent Experiments on Li Pellet Injection into Heliotron E; Aug. 1996*
- NIFS-429 N. Noda, V. Philipps and R. Neu,  
*A Review of Recent Experiments on W and High Z Materials as Plasma-Facing Components in Magnetic Fusion Devices; Aug. 1996*
- NIFS-430 R.L. Tobler, A. Nishimura and J. Yamamoto,  
*Design-Relevant Mechanical Properties of 316-Type Stainless Steels for Superconducting Magnets; Aug. 1996*
- NIFS-431 K. Tsuzuki, M. Natsir, N. Inoue, A. Sagara, N. Noda, O. Motojima, T. Mochizuki, T. Hino and T. Yamashina,  
*Hydrogen Absorption Behavior into Boron Films by Glow Discharges in Hydrogen and Helium; Aug. 1996*
- NIFS-432 T.-H. Watanabe, T. Sato and T. Hayashi,  
*Magnetohydrodynamic Simulation on Co- and Counter-helicity Merging of Spheromaks and Driven Magnetic Reconnection; Aug. 1996*